Physics – Uspekhi **63** (3) 269 – 288 (2020)

REVIEWS OF TOPICAL PROBLEMS PACS numbers: 02.70.Uu, **73.20. – r**, 73.43.Cf, 75.10.Hk, 75.70.Ak

Localized structures in magnetic systems without the center of inversion

A B Borisov

DOI: https://doi.org/10.3367/UFNe.2019.02.038701

Contents

Abstract. The main theoretical and experimental results of the study of magnetic skyrmions in films of isotropic chiral magnets are considered. A significant part of the paper presents new results that were not included in previous monographs and reviews. Skyrmions are formations characterized by a quantized topological number. They attract considerable attention of researchers due to their dynamics in external fields, which has promising features in terms of applications in spintronics. Special attention is given to the structure and interaction of 3D skyrmions, and a new magnetic structure — the chiral bobber — is considered.

Keywords: skyrmion, chiral magnet, helimagnet, chiral bobber

1. Introduction

The term 'skyrmion' was proposed by Tony Skyrme in the 1960s to refer to a solution with a topological singularity in a nonlinear sigma model from the field of elementary particle physics [1–3]. Since then, many different versions of the concept of 'skyrmions' have been used to designate states and localized particle-like excitations in various condensed matter, including two-dimensional electronic gases with the quantum Hall effect [4], Bose–Einstein condensates [5], liquid crystals [6], and superfluid ^{3}He.

A B Borisov Mikheev Institute of Metal Physics,
Ural Branch of the Russian Academy of Sciences,
ul. S. Kovalevskoi 18, 620108 Ekaterinburg, Russian Federation;
Institute of Natural Sciences and Mathematics, Ural Federal University
named after the first President of Russia B N Yeltsin,
ul. Kuibysheva 48, 620026 Ekaterinburg, Russian Federation
E-mail: borisov@imp.uran.ru

Received 14 February 2019, revised 24 February 2019
Uspekhi Fizicheskikh Nauk **190** (3) 291 – 312 (2020)
Translated by G A Sorokin; edited by V L Derbov

The first skyrmions were observed in 1983 [7] (see also monograph [8]) in the chiral superfluid A-phase of ^{3}He where the Cooper pairing of atoms occurs in the state with spin $S = 1$ in the p state with orbital moment $L = 1$. Experiments using the nuclear magnetic resonance (NMR) method clearly indicated the existence of new superfluid vortices with a velocity $\mathbf{v}_s$, which, unlike the velocity of vortices in ^{4}He, was not determined by the phase gradient and was nonsingular on the vortex axis. Quantization of the circulation of these vortices was determined by the distribution of the field of vector $\mathbf{l}$ ($|\mathbf{l}| = 1$) associated with the orbital part of the order parameter and its topology. In the cross-section plane of the vortex, the field $\mathbf{l}$ takes all the values on the sphere S^2 twice. It is this that leads to the formation of new vortices in superfluid ^{3}He-A, called skyrmion vortices. The topology of such particle-like solitons, including three-dimensional (3D) solitons, merons, and hopfions, was discussed in [8, 9].

However, in recent years, skyrmions have been very actively investigated in the scope of solid-state magnetism, where new spin structures are also called skyrmions. These textures are magnetic vortices but, unlike the previously studied vortex structures [10–12], they are formed in magnetic crystals without a center of inversion (chiral ferromagnets). In such systems, the competition between the exchange interaction and the Dzyaloshinskii–Moriya interaction caused by the spin-orbital coupling leads to the appearance of noncollinear or nonplanar spin structures, such as magnetic vortices, domain walls, and helices.

In theory, magnetic vortices as structures with finite energy were predicted in noncentrosymmetric magnetic crystals [13] as early as 1989 (see also [14]). Such vortices were later called magnetic skyrmions [15]. Somewhat later, by analogy with the Abrikosov vortex lattice in type II superconductors, Bogdanov et al. pointed out the possibility of forming a skyrmion lattice in a certain range of magnetic fields in a number of noncentrosymmetric crystals [16–19]. In

2010, in experiments with an $Fe_{0.5}Co_{0.5}Si$ thin film using transmission electron microscopy (TEM) methods, Tokura's group found a stable 2D skyrmion lattice in a wide temperature range down to almost zero temperature [20]. This work initiated an avalanche of publications on the study of skyrmions and other textures in bulk and thin-film chiral magnets.

Skyrmions are characterized by a quantized topological number and attract considerable attention of researchers, since their exotic dynamics in external fields have promising properties for applications in spintronics. Today, the literature on the structure, physical properties, and dynamics of skyrmions, including technical applications, is rich (see monographs [21–25] and reviews [26–31]).

This review presents the main theoretical and experimental results on the study of magnetic skyrmions in films of isotropic chiral magnets. A significant part of the review is devoted to new results that were not included in previous monographs and reviews. Unfortunately, for a number of reasons, F N Rybakov, who with his colleagues made a decisive contribution to our collaboration, could not be a coauthor of this review.

Section 2 provides a brief introduction to helicoidal structures in chiral magnets, including their theoretical description based on the Ginzburg–Landau functional and the results of the first experiments for detecting one-dimensional helical structures.

Section 3 provides a theoretical description of the skyrmion and 2D skyrmion lattice in a bulk crystal as well as the results of observations by Tokura's group of skyrmion lattices in real space in a thin film of $Fe_{0.5}Co_{0.5}Si$ using TEM methods. The experimental phase diagram of magnetic structures in a thin film obtained by Tokura's group demonstrated its significant *differences from the phase diagrams in a bulk crystal*.

The first 3D calculations of modulated chiral states in thin films of cubic helimagnets are presented in Section 4. It is shown that conical modulations of helicoids and skyrmion lattices provide a specific mechanism for stabilizing these structures in a wide range of magnetic fields at low temperatures.

In Section 5, a new phase (a stack of spin helices) in a certain range of magnetic fields and film thicknesses of an isotropic helimagnet is predicted using computer simulation.

The structure and properties of the new particle-like state — the so-called chiral bobber predicted in [32] — are discussed in Section 6. As distinct from the previously known magnetic localized structures — domain walls, helices, skyrmions, vortices — a thermodynamically stable chiral bobber is formed on the phase interface or on the surfaces of chiral magnets.

Section 7 presents the results of experimental detection of a chiral bobber in thin plates of an FeGe helimagnet using off-axis electronic holography. A new concept of magnetic solid state memory is proposed based on encoding the data stream with a chain of alternating magnetic skyrmions and chiral bobbers, which play the role of bits 1 and 0.

Experimental and theoretical studies of the interaction of skyrmions with each other and with the edges of samples in nanostrips of an FeGe chiral magnet are described in Section 8. It is shown that in magnetic fields exceeding a certain critical value the nature of the interaction of skyrmions changes from attraction to repulsion, which is quantitatively consistent with the results of micromagnetic simulation.

Section 9 presents some results of the theory of 2D magnetic helical textures of the FeGe helimagnet experimentally discovered in [33]. Analytical and numerical methods made it possible to determine the structure of these helical textures and predict spiral lattices.

2. Helicoidal structures in cubic chiral magnets

Let us first consider localized magnetic structures in crystals without a center of symmetry. Typical examples are manganese silicide MnSi (the first thoroughly studied magnetic system without an inversion center [26]), FeGe, and $Fe_{0.5}Co_{0.5}Si$. Let us recall that the center of symmetry of an elementary cell is a mathematical point characterized by the fact that, on a line drawn through this point, atoms of the same type are located at the same distances on both sides of it. The MnSi compound is a ferromagnetic 3d-metal with a cubic crystal structure $B20$ without a center of symmetry (spatial group $P2_13$) (Fig. 1). This compound exists in two versions (right-handed and left-handed) which are mirror images of each other. Such crystals are called enantiomorphic.

Atoms in the right-handed modification of MnSi have coordinates

$$(x,x,x),\quad \left(\frac{1}{2}+x,\,\frac{1}{2}-x,\,-x\right),\quad \left(-x,\,\frac{1}{2}+x,\,-x\right),$$
$$\left(\frac{1}{2}-x,\,-x,\,\frac{1}{2}+x\right),$$

where x is measured in units of the lattice constant: $x_{Mn}=0.137$, $x_{Si}=0.845$. The left-handed modification corresponds to the replacement $x\to 1-x$. Magnets without a center of symmetry are often called chiral or helicoidal. A microscopic model of a Heisenberg ferromagnet is used to theoretically describe the magnetic structures of the MnSi compound with energy of the form

$$E=\sum_i\sum_{j(j\neq i)}\left(-J_{ij}\mathbf{s}_i\mathbf{s}_j+\mathbf{D}_{ij}[\mathbf{s}_i\times\mathbf{s}_j]\right)-g\mu_B\mathbf{H}\sum_i\mathbf{s}_i\,, \qquad (1)$$

which includes the exchange interaction of spins $\mathbf{s}_i$ on the ith node of the lattice with exchange integrals J_{ij}, the Dzyaloshinskii–Moriya (DM) interaction with the anisotropic vector $\mathbf{D}_{ij}$, and the interaction with the external magnetic field $\mathbf{H}$ (μ_B is the Bohr magneton, g is the gyromagnetic ratio). In typical magnets without a center of symmetry, the Heisenberg exchange interaction between adjacent spins has the form

$$-J\mathbf{s}_i\mathbf{s}_j,\qquad |\mathbf{s}_i|=1,\qquad J>0,$$

and in the ground state lines up the spins in one direction (Fig. 2a) [25]. In cubic crystals with a $B20$ crystal structure,

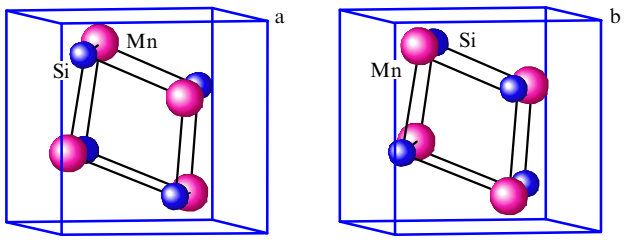

Figure 1. (Color online.) Crystal structure of (a) right-handed and (b) left-handed modifications of MnSi.

due to the loss of inversion symmetry, a nontrivial DM interaction occurs [34, 35] due to the spin-orbital coupling of neighboring atoms: $H = \lambda(\mathbf{S}_1\mathbf{L}_1 + \mathbf{S}_2\mathbf{L}_2)$. For the two nearest spins, the DM interaction has a simple form: $\mathbf{D}_{12}[\mathbf{s}_1 \times \mathbf{s}_2]$ [35]. The constant vector $\mathbf{D}_{12}$ is expressed in terms of matrix elements of the operators of the orbital moments of electrons ($\mathbf{L}_1$, $\mathbf{L}_2$) in the basis of atomic orbitals and depends on the difference between the energies of atoms in excited and ground orbital states. This interaction is minimized for mutually perpendicular neighboring spins (Fig. 2b). As a result, due to the competition of Heisenberg and DM interactions, a nonuniform ground state is established in $B20$ structures — a helical (screw-shaped) structure [36] (Fig. 3a).

The spin structure in the unit cell of MnSi is described by a superposition of four helices:

$$\mathbf{s}_i = \mathbf{a}_i \cos(\mathbf{kr}) + \mathbf{b}_i \sin(\mathbf{kr}), \qquad i = 1, 2, 3, 4,$$

where $\mathbf{r}$ is the position of the atom in the cell, $\mathbf{a}_i$, $\mathbf{b}_i$ are unit vectors, and $\mathbf{a}_i\mathbf{b}_i = 0$. It is seen that the spins in each magnetic sublattice rotate in a plane perpendicular to the vector $\mathbf{c}_i = \mathbf{a}_i \times \mathbf{b}_i$. The wave vector $\mathbf{k}$ sets not only the direction of modulation but also the change in the phase of rotation of the spins when moving from the initial cell to the neighboring ones. The modulation period depends on the temperature, and it is incommensurate with the lattice period. Therefore, helical structures are often called long-period or incommensurable. Review [27] and book [37] were among the first reviews and monographs that set out the theory of long-period structures. A microscopic theory of MnSi helical structures with energy (1) is proposed in [38], where, in particular, it is shown that in the approximation of the nearest neighbors, the modulus of the vector $\mathbf{k}$ is expressed in terms of the components of the Dzyaloshinskii–Moriya vector $\mathbf{D} = \mathbf{D}_{12}$:

$$|\mathbf{k}| = \frac{2(D_x - 2D_y + D_z)}{3J}, \quad \mathbf{D}_{12} \equiv \mathbf{D} = (D_x, D_y, D_z).$$

In [38], the relationship between microscopic and phenomenological theory is established. It is shown that, in the continuum approximation, the energy (1) of the helical structure takes the form

$$E = \int \mathrm{d}\mathbf{r} \left[J_1 \frac{\partial \mathbf{s}}{\partial x_i} \frac{\partial \mathbf{s}}{\partial x_i} + D_1(\mathbf{s}\ \mathrm{rot}\ \mathbf{s}) + E_{\mathrm{skew}} \right].$$

The first two terms coincide with the energy in a Ginzburg–Landau-type phenomenological theory with parameters

$$J_1 = \frac{3J}{4}, \qquad D_1 = D_x - 2D_y + D_z.$$

The skew energy E_{skew} is proportional to

$$J\left(12 + 2\left(\frac{D_x + D_y}{J}\right)^2\right)$$

and is associated with the skews of neighboring spins (or with the disorientation of the rotation axes $\mathbf{c}_i$ ($i = 1, 2, 3, 4$) of four helices with different positions of Mn in the unit cell).

A model used for a macroscopic description of magnetic structures in compounds $B20$ has the energy density:

$$E = A \frac{\partial \mathbf{n}}{\partial x_i} \frac{\partial \mathbf{n}}{\partial x_i} + D\mathbf{n}\ \mathrm{rot}\ \mathbf{n} - M\mathbf{Hn}, \tag{2}$$

where $\mathbf{n} = (\sin\theta\cos\Phi,\ \sin\theta\sin\Phi,\ \cos\theta)$ is the unit vector along the direction of magnetization, M is the spontaneous magnetization of the material, and A is the exchange interaction constant.

The theoretical study of one-dimensional chiral structures was carried out in papers [16, 34, 35]. In the absence of a field, the ground state is a helix with the vector $\mathbf{k} = (0, 0, k)$ and the period L_D:

$$\theta = \frac{\pi}{2}, \qquad \Phi = kz, \qquad k = \frac{|D|}{2A}, \qquad L_D = \frac{2\pi}{k},$$

with the distribution of the magnetization

$$\mathbf{n} = \big(\cos(kz), \sin(kz), 0\big) \tag{3}$$

and the energy density

$$E_{\mathrm{hel}} = -\frac{H_D M}{2}, \qquad H_D = \frac{D^2}{2AM},$$

as shown in Fig. 3a, b where the arrows show the directions of the vector $\mathbf{n}$ (3) in the planes $z = \mathrm{const}$, in which the magnetic moments are codirectional. Magnetic moments change their orientation when going from layer to layer, forming a helical wave with the period L_D determined by the constants of exchange interaction and spin-orbit coupling. When the latter

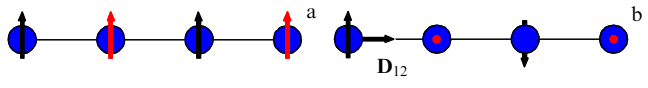

Figure 2. (Color online.) Main interactions in chiral magnets: (a) ferromagnetic exchange, (b) noncollinear DM interaction. (From [25].)

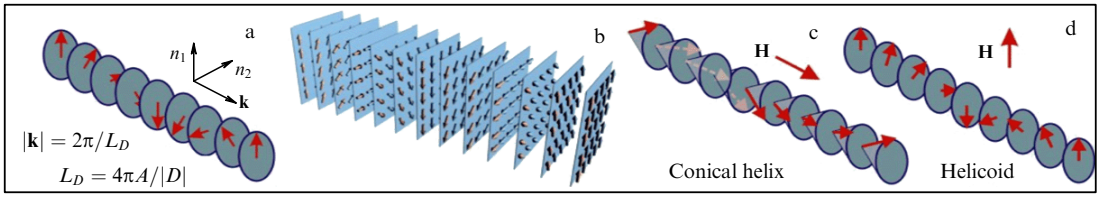

Figure 3. Schematic representation of various modulated states in chiral magnets: (a) a spin spiral in the absence of a magnetic field with a wave vector $\mathbf{k}$ along the z axis, (b) the location of the helix in planes. Under the influence of a magnetic field, the helix (a) is transformed either into a conical helix (c) with an inclined magnetization and a wave vector along the magnetic field or into a longitudinal helicoid (d).

decreases, L_D goes to infinity, which corresponds to the transition to a homogeneous ferromagnetic state. In various types of *B*20 magnets, the structure period L_D varies from a few nanometers to several hundred nanometers. In cubic helimagnets in the absence of a field, the ground states will also all be helicoidal structures that are obtained from (3) by simultaneous rotation of the spin and coordinate spaces.

In a magnetic field, there are two ground states that differ in the directions of the magnetic field and magnetization. In the magnetic field $\mathbf{H} = (0, 0, H)$ parallel to the helix vector, the spins deviate to the direction of the field, and the simple helix is transformed into a conical helix (forming a conical phase). In the conical phase (Fig. 3c), the distribution of magnetization is as follows:

$$\cos\theta = \frac{H}{H_D}\,, \quad \Phi = \frac{2\pi}{L_D}\,z \tag{4}$$

with energy density

$$E_{\text{cone}} = -\frac{H^2 + H_D^2}{2H_D}\,M\,. \tag{5}$$

In the critical field $H = H_D$, the conical phase transforms into a ferromagnetic state in which all spins are unidirectional with the field vector, and the energy density is expressed as $E_{\text{sat}} = -HM$ $(H \geqslant H_D)$. From a comparison of energy densities, it follows that the field-dependent transition between the conical and ferromagnetic phases is a second-order phase transition.

If the magnetic field $\mathbf{H} = (0, 0, H)$ is perpendicular to the helix vector $\mathbf{k} = (k, 0, 0)$ and $\Phi = \pi/2$ (as on the Bloch domain wall), then the vector $\mathbf{n}$ lies in the plane yz,

$$\mathbf{n} = \mathbf{e}_y \sin\theta(x) + \mathbf{e}_z \cos\theta(x)\,,$$

where the angle $\theta(x)$ defines the *modulated helicoidal* structure (Fig. 3d), the explicit form of which,

$$\cos\frac{\theta}{2} = \operatorname{sn}\left(\frac{2\sqrt{H}x}{mL_D\sqrt{H_D}}, m\right), \qquad \sin\frac{\theta}{2} = \operatorname{cn}\left(\frac{2\sqrt{H}x}{mL_D\sqrt{H_D}}, m\right), \tag{6}$$

is found by integrating Euler equations

$$2A\frac{\mathrm{d}^2\theta}{\mathrm{d}x^2} - HM\sin\theta = 0$$

for the functional (2). Here, $\operatorname{sn}(x, m)$ and $\operatorname{cn}(x, m)$ are Jacobi elliptic functions with the modulus m $(0 \leqslant m \leqslant 1)$. The parameter m is determined by minimizing the average energy $\bar{E}$ per period L of the structure:

$$\bar{E} = \frac{1}{L}\int_0^L E\,\mathrm{d}z = MH\left(1 - \frac{2}{m^2} + \frac{4E(m)}{K(m)}\right) - \frac{D\pi}{mK(m)}\sqrt{\frac{HM}{2A}}\,, \tag{7}$$

where $K(m)$ and $E(m)$ are complete elliptic integrals of the first and second kind, respectively. Direct calculations show that the average energy is minimal if m satisfies the implicit equation

$$m\pi\sqrt{H_D} - 4\sqrt{H}E(m) = 0\,. \tag{8}$$

Then, the equilibrium average energy $\bar{E}$ and the period of the helicoid L are expressed as

$$\begin{aligned} \bar{E} &= \frac{1}{m^2}\,H(m^2 - 2)M\,, \\ L &= \frac{1}{\pi}\sqrt{\frac{H_D}{H}}\,mL_DK(m) = \frac{4}{\pi^2}\,L_DK(m)E(m)\,. \end{aligned} \tag{9}$$

Equation (8) has a solution under the condition

$$\sqrt{\frac{H_D}{H}} > \frac{4}{\pi}\,.$$

Formulas (7)–(9) give a complete analytical description of the helicoidal structure. The period of the helicoid continually increases from $L = L_D$ at $H = 0$ (since $E(0) = K(0) = \pi/2$ at $m = 0$) up to infinity in the critical field H_{c} (at $m = 1$):

$$H_{\text{c}} = \frac{H_D\pi^2}{16}\,. \tag{10}$$

In this case, the explicit form of the helicoidal structure changes from the sinusoidal one,

$$\cos\theta = \cos\left(\frac{2\pi}{L_D}\,x\right), \qquad H = 0\,,$$

to the localized one,

$$\cos\theta = 1 - \frac{2}{\cosh\left[\pi^2 x/(2L_D)\right]^2}\,, \qquad H = H_{\text{c}}\,.$$

In magnetic fields $H > H_{\text{c}}$, equation (8) has no solutions. The ground state is $\theta = 0$ (ferromagnetic ordering).

In a number of experimental papers (e.g., [39–45] and references therein), helical structures in compounds $Fe_{1-x}Co_xSi$ and MnSi have been studied using neutron scattering. In an $Fe_{1-x}Co_xSi$ isotropic helimagnet, a helical structure with the vector $\mathbf{k} = (k, 0, 0)$ along the direction [100] and with the magnetization $\mathbf{M} = |\mathbf{M}|(0, \sin(kx), \cos(kx))$ [46] was observed using the TEM method. Unlike neutron scattering, which provides information about the magnetic structure in the momentum space, the TEM method allows the magnetic structure to be visualized in real space. This has the advantage that separate spin textures, dislocations of the skyrmion crystal, etc. can be observed with changes in temperature and magnetic field. TEM involves studying thin samples using an electron beam. When a flow of electrons irradiates a ferromagnet, the Lorentz force induced by the magnetization component orthogonal to the incident electron beam deflects the beam, after which it focuses on the imaging device. The transport intensity equation (TIE) is used to process the TEM results [47].

The helical structure $Fe_{1-x}Co_xSi$ shown in Fig. 4 (below the Néel temperature $T_{\text{N}} = 38$ K) is obtained in [46] using the TEM method with an electron beam perpendicular to the film plane. The image in Fig. 4a clearly shows the distribution of magnetization in the periodic structure of the strips (the strips are orthogonal to the axis [100]). The direction and amplitude of the magnetization are represented by changes in color and brightness according to the color map (lower right corner of Fig. 4a). Green and purple pairs of strips represent areas with opposite magnetic orientation; the darker regions correspond to a lower local magnetization amplitude. Sinusoidal modula-

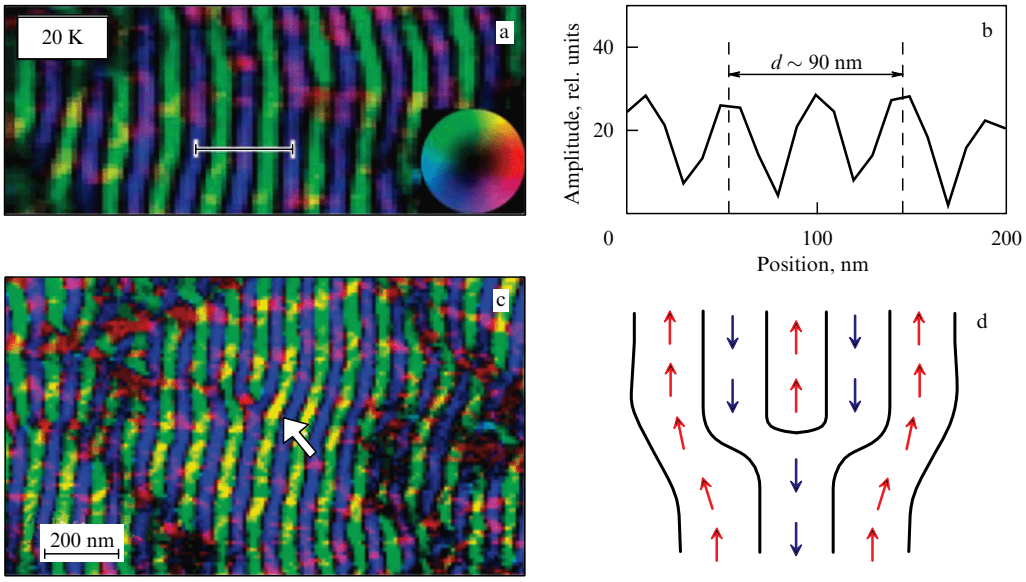

Figure 4. (Color online.) Helical spin order in $Fe_{1-x}Co_xSi$ (see explanations in the text).

tion in Fig. 4b (the profile of the magnetization amplitude along the bright line in Fig. 4a) indicated a helix spin ordering with a period of 90 nm along the [100] axis, which is in good agreement with neutronographic results [48–50].

Another interesting feature of the magnet structure $Fe_{1-x}Co_xSi$, according to [46], is the presence of topological magnetic defects. Experimental results revealed defects in the helical structure that are similar to grains and dislocations in the crystal lattice [51]. Figure 4c shows the magnetization distribution in the sample, consisting of several areas separated by wavy lines with dark contrast. Within each region (magnetic domain), there is a periodic order of spins with a given direction of the helix axis. Most of the neighboring regions are characterized by a slight disorientation of the helix axis, but with no change in the period of the helix. Spin strips can be seen even inside dark-contrast areas where the order of spins in the helix is less regular. Therefore, the wavy dark-contrast region can be called the helical boundary of the magnetic domain. After the sample was heated to the temperature $T > T_N$ and then cooled to the initial temperature (20 K), new domain structures appeared, which differed from the previous ones in shape and size. Domain structures are also sensitive to magnetic fields. Figure 4d schematically shows the magnet edge dislocation which is located in the area indicated by the arrow in Fig. 4c.

3. Two-dimensional skyrmion lattices

As mentioned in the Introduction, two-dimensional magnetic vortices — skyrmions in crystals without an inversion center — were first predicted [13, 14] in 1989–1990 by analogy with vortices in type II superconductors. In such magnets, localized structures with finite energy can exist, which are stabilized by the negative DM interaction. In [16], the structure of isolated skyrmions at different values of the magnetic field and the easy-axis anisotropy parameter in chiral magnets of the crystal classes D_n, C_{nv} ($n = 3, 4, 6$) is investigated using numerical integration of the Lagrange–Euler equations for the energy functional (2). Profiles of skyrmions were defined using the substitutions

$$\theta = \theta(\rho), \qquad \Phi = \phi + \frac{\pi}{2}, \tag{11}$$

$$\theta = \theta(\rho), \qquad \Phi = \phi \tag{12}$$

and asymptotic conditions $\theta(\infty) = 0$, $\theta(0) = \pi$ in the polar coordinate system (ρ, ϕ). Such structures are called Bloch and Néel skyrmions, respectively.

From asymptotic conditions $\mathbf{n} \to (0, 0, -1)$ (for $\rho \to \infty$), it follows that we can consider this field on an extended plane R^2 to which an infinitely remote point (∞) is attached. Such a plane is isomorphic to a two-dimensional sphere, in the symbolic notation $S_R^2 = R^2 \cup \infty$. On the other hand, the field $\mathbf{n}(x, y)$ takes values on the unit sphere S_n^2 ($\mathbf{n}^2 = 1$). In other words, the function $\mathbf{n}(x, y)$ maps the sphere S_R^2 to the sphere S_n^2. In topology, the set of sphere-to-sphere mappings is divided into equivalence classes (homotopy classes), and continuous deformation can translate mappings only within a single class. Each homotopy class can be assigned an integer Q, called a topological charge, which does not change when the field is continuously deformed. For a field of a unit vector, the topological charge is defined by the expression

$$Q = \frac{1}{4\pi} \int \sin\theta (\partial_x \theta \, \partial_y \Phi - \partial_y \theta \, \partial_x \Phi) \, \mathrm{d}x \, \mathrm{d}y \, .$$

Simple calculations show that the topological charge for a skyrmion has the form

$$Q = \frac{1}{4\pi} \int \sin\theta \, \mathrm{d}\theta \, \mathrm{d}\Phi = -\frac{1}{2} \big(\cos\theta(\infty) - \cos\theta(0)\big) = -1 \, .$$

In addition, in [16, 18, 52], a two-dimensional skyrmion lattice was predicted, similar to the Abrikosov vortex lattice in type II superconductors. The hexagonal lattice cells were approximated by circular cells, and the energy of the spin texture of a unit area

$$w = \frac{2}{R^2} \int_0^R E\big(\theta(r), r\big) \, \mathrm{d}r$$

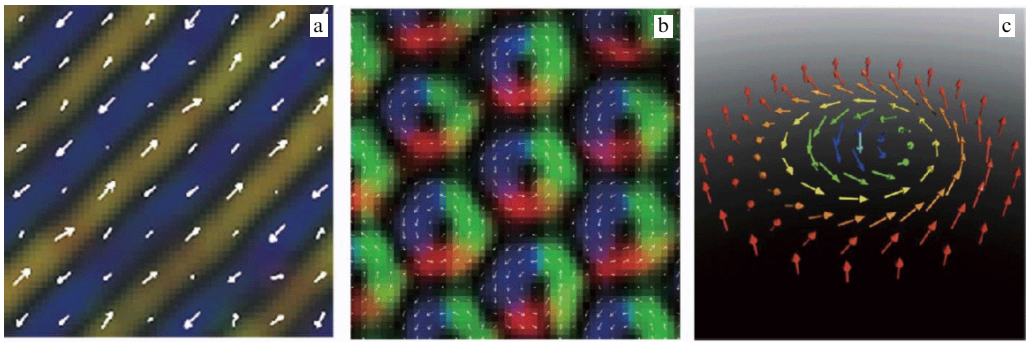

Figure 5. (Color online.) Topological spin textures in $Fe_{0.5}Co_{0.5}Si$ film. (a) Helical and (b) skyrmion structures predicted by simulations using the Monte Carlo method. (c) Diagram of the spin configuration of skyrmions.

was numerically studied in this approximation under boundary conditions

$$\theta(0) = \pi\,, \qquad \theta(R) = 0\,.$$

Here, $E(\theta(r), r)$ is the energy density of the magnet, R is the radius of the cell. The results of the calculations give the equilibrium radius R for the vortex cell, which depends on the external magnetic field and the anisotropy parameter. Finally, in [17], using a model that allows for changes in spontaneous magnetization (a typical example is metal magnets), it is shown that skyrmion textures as ground states can exist in many chiral magnets, including those on the surfaces of thin films and in bulk samples.

Experiments on small-angle neutron scattering in MnSi [53] and $Fe_{0.5}Co_{0.5}Si$ [54] compounds have shown that, in a certain limited range of temperature and magnetic field parameters, six peaks of Bragg reflections from a hexagonal lattice strictly perpendicular to the magnetic field are observed for all orientations of the magnetic field relative to the lattice of atoms. In [53], it is suggested that they correspond to a new magnet phase called the A-phase. The magnetization in this phase can be approximated by a superposition of the magnetizations of three helicoidal structures that are perpendicular to the external field and rotated 120° relative to each other. The spin texture with the lowest energy can be considered a 2D lattice of magnetic vortices for which the magnetization in the center is directed opposite to the vector of the applied field. The authors of [53], after analyzing theoretical and experimental data, concluded that the skyrmion lattice is stabilized by thermal fluctuations in the A-phase.

A two-dimensional skyrmion lattice in real space was first observed in a thin $Fe_{0.5}Co_{0.5}Si$ film using TEM methods [20]. The results of Monte Carlo simulation in [20] for a discrete version of the Hamiltonian in an external magnetic field predict that the helical structure will transform into a two-dimensional skyrmion lattice when the film thickness is close to the period of the helical structure. Observations of TEM in the zero field at temperatures below the magnet transition temperature (38 K) clearly show the strip structure (Fig. 5a) with a transverse magnetization component and a period of 90 nm. The helical structure is formed along the directions [100] or [010]. If the magnetic field (50 mT) is applied normally to the plate, then, as predicted in the simulation, a two-dimensional hexagonal lattice of skyrmions is observed (Fig. 5b). A diagram of the spin configuration of skyrmions on an enlarged scale is shown in Fig. 5c. The lattice period is of the same order of magnitude as the period of the original strip structure — 90 nm. Every skyrmion has a gain in energy of DM interaction. The areas between skyrmions give a gain in the energy of the magnetic field. Thus, a tightly packed hexagonal lattice of skyrmions provides a gain in both energies. Twisting of spins counter-clockwise in the region of each skyrmion reflects the sign of the DM interaction for chiral magnets. As follows from the simulation results, the spins in the black centers of the skyrmions are directed downwards.

Field and temperature dependences of spin textures are also investigated in [20]. First, the isothermal change in the spin texture in a magnetic field applied along the normal (001) to the surface of the film is studied. The configuration of the magnet structure in the absence of a field coincides with the helical structure along the direction (100). When the magnetic field increases to 20 mT, a fragment of the hexagonal lattice of skyrmions is generated in the structure of the strips. When the field is further increased to 50 mT, the strip domains are completely transformed into a hexagonal lattice of skyrmions that occupies the entire surface (001) of the sample except for the area containing the dislocation. The skyrmion lattice is replaced by a homogeneous ferromagnetic alignment of spins in a magnetic field of the order of 80 mT. A similar pattern of skyrmion generation is observed when the temperature changes in a constant magnetic field (50 mT) directed along the normal to the surface of the film. The texture of the spin strips observed at 5 K transforms at 15 K into a mixed structure of strips and skyrmions, and then at 25 K a hexagonal lattice of skyrmions is formed. At 40 K, the inhomogeneous spin ordering disappears.

The experimental phase diagram of the spin textures in a thin $Fe_{0.5}Co_{0.5}Si$ film in Fig. 6 is in good agreement with the results of the Monte Carlo simulation of the two-dimensional (2D) model (2). The magnetic field and temperature are normalized using arbitrary constants B_C and T_C. The colored strips on the right side of the phase diagram show the skyrmion density in units of 10^{-12} m^2 per d^2, where d is the wavelength of the helicoid. The dashed lines represent the phase interfaces between the skyrmion crystal (SC), the helicoidal structure (HL), and the ferromagnet (FM). There is good agreement between the experimental data and the results of numerical simulation not only for the interfaces between the helicoidal phase and the skyrmion crystal but also for the regions of coexistence of the HL, FM, and SC states. Even in a weak magnetic field, the transition to the skyrmion phase depends on the temperature.

In addition, in [20], *significant differences between phase diagrams in a thin film and in a bulk crystal* were noted. The

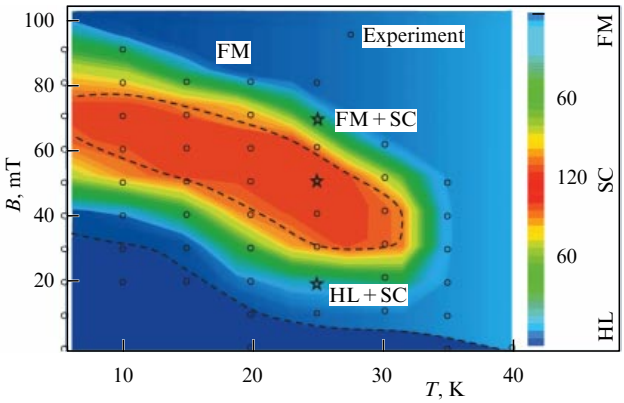

Figure 6. (Color online.) Experimental phase diagram of the magnetic structure in a thin $Fe_{0.5}Co_{0.5}Si$ film on the magnetic induction–temperature ($B-T$) plane.

skyrmion phase of the film on the $B-T$ plane occupies a relatively large area. In a bulk crystal, the skyrmion phase exists only in a narrow window on the $B-T$ plane: at magnetic induction of the order of 10 mT and temperatures of 35–40 K [43]. The critical field in the ferromagnetic region of the film increases in comparison with that in the three-dimensional case (up to 100 mT at 5 K). It is interesting that the SC phase in the film can be obtained, which is important, using a magnetic field perpendicular to the film even at low temperatures when the thermal fluctuations are small.

4. Three-dimensional skyrmions in thin films of chiral magnets

According to the theory developed by Bogdanov et al. [16, 18, 55], quasi-two-dimensional skyrmions in bulk chiral magnetics with relatively weak crystallographic anisotropy can only exist in a metastable state. The energy of skyrmions is always higher than the energy of the conical phase, which dominates in bulk samples over almost the entire range of magnetic fields and temperatures. This conclusion is consistent with many experimental studies of chiral magnets in which skyrmions were not observed. The only exception is the A-phase, the high-temperature region of the phase diagram (slightly below the uniform ordering temperature), in which skyrmions are stabilized by thermal fluctuations.

Theoretical models [18, 55–57] predict that in bulk magnets skyrmions can also be stabilized by strong cubic or uniaxial anisotropy (including 'easy plane' type anisotropy induced by magnetoelastic interaction) or by another special crystal symmetry that suppresses the formation of a conical phase. Experimental observations of the magnetic properties of skyrmions in thin films of cubic helimagnets [20, 58–62] in the absence of induced anisotropy clearly differed from the magnetic properties of skyrmions in bulk cubic helimagnets, where skyrmions can only exist as metastable states. In this regard, the first three-dimensional calculations of chiral modulated states in thin films of cubic helimagnets were performed [63]. As a result, the physical mechanism underlying the formation of skyrmions in magnets without an inversion center was elucidated.

In numerical calculations, expression (2) was used for the energy density of a cubic ferromagnet without an inversion center, which does not take into account the intrinsic and

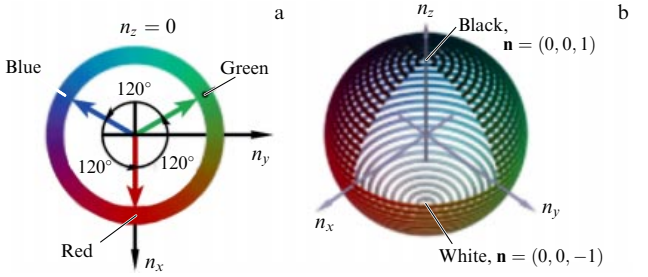

Figure 7. (Color online.) Directions of the vector $\mathbf{n}$ in the section $n_z = 0$ (a) and on the sphere (b) shown in different colors.

externally induced energy of magnet anisotropy

$$Kn_z^2$$

as well as magnetodipole interaction, both of which are weak due to the stabilizing effect of DM interaction [64]. A film with thickness L infinite in the x and y directions bounded by parallel planes $z = \pm L/2$ was considered. Numerical solutions were obtained by direct minimization of the energy functional with free boundary conditions along the z axis ($\partial_z\theta = 0, \partial_z\Phi = 2\pi/L_D$) and periodic boundary conditions in the (x, y) plane. This leads to an equilibrium inhomogeneous distribution of magnetization in the film, which depends on three spatial variables and two parameters: the dimensionless magnetic field H/H_D and the *confinement parameter* L/L_D. In [63], a special calculation algorithm was developed in the CUDA [1] architecture for Nvidia graphics cards, and a nonlinear method of conjugate gradients was used to minimize the energy functional. The minimization results were checked for compatibility with the Euler–Lagrange equations.

Here and hereafter, the color map defined in Fig. 7 is used to indicate the direction of the vector $\mathbf{n}$ in the figures. The results of numerical simulation are shown in Figs 8 and 9.

The equilibrium configuration of the 3D skyrmion lattice is very different from the 2D skyrmion lattice in bulk helimagnets. The magnetization distribution $\mathbf{n}$ in a cylindrical coordinate system, depending on three variables ρ, ϕ, z, demonstrates complex three-dimensional modulations of the z plane (see also the video in [65] illustrating the conical and helicoidal magnetic structures as well as the structure of the skyrmion in the film). In numerical modeling, trial functions

$$\theta = \theta(\rho)\,, \qquad \Phi = \phi + \frac{\pi}{2} + \frac{2\pi}{L_D}\,z \tag{13}$$

provide a good approximation of solutions for isolated and lattice 3D skyrmions. In formulas (13), the dependence of the field Φ on ρ and of the angle θ on z is neglected, and the term $2\pi z/L_D$ is taken the same as in the conical phase (4).

The energy of a skyrmion in approximation (13) was calculated by the formula

$$E_s = \frac{1}{AL_D}\int_0^{2\pi} \mathrm{d}\phi \int_{-L/2}^{L/2} \mathrm{d}z \int_0^{\infty} (E - E_0)\rho\,\mathrm{d}\rho\,, \tag{14}$$

[1] CUDA (Compute Unified Device Architecture) — hardware and software architecture for parallel computing that improves computing performance by using Nvidia GPUs.

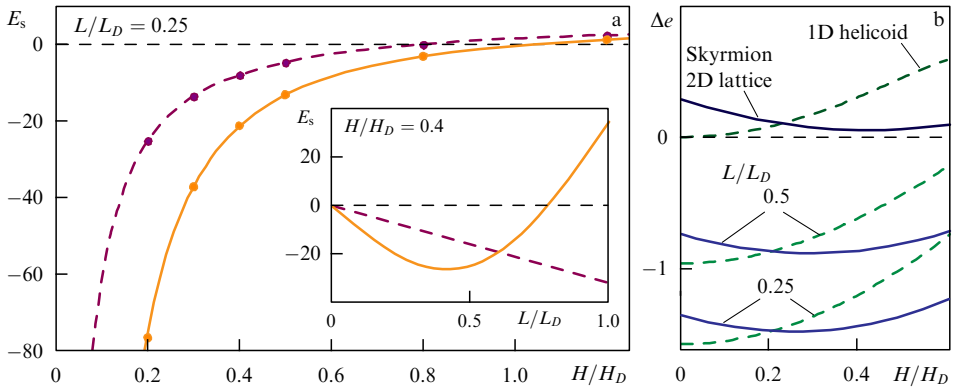

Figure 8. (Color online.) (a) Dependence of equilibrium energy (14) for isolated 3D skyrmions (solid curve) and for 2D skyrmions uniform along the z axis (dashed curve) on the field H/H_D. (b) The dependence of the energy difference Δe between the skyrmion lattice and the conical phase (solid blue curve) and between the helicoidal and conical phases (dashed green curve) on the applied field.

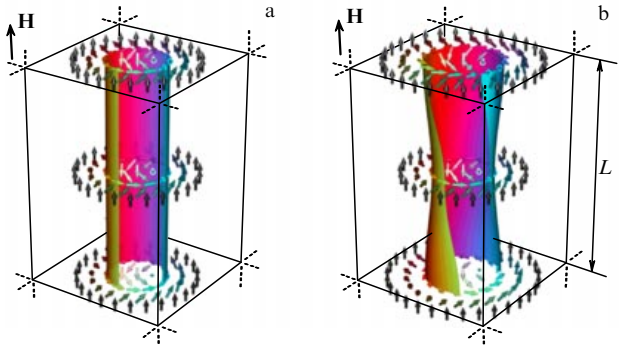

Figure 9. Schematic representation of skyrmion tubes. (a) Vector fields and isosurfaces $n_z = 0$ for a skyrmion tube with uniform magnetization along the symmetry axis. (b) Skyrmion tube with three-way inhomogeneous magnetization and rotations of magnetic moments induced by the film surface. $n_z > 0$, $n_x < 0$ in sections $z = \text{const}$.

where $E_0 = -HM$ is the energy density of the saturated state. The results shown in Fig. 8a demonstrate that in a wide range of parameters, $0.2 < H/H_D < 1$, the energy of isolated 3D skyrmions is less than that of 2D skyrmions homogeneous along the z axis. The film thickness is $L/L_D = 0.25$. In the inset in Fig. 8, the dependence of the skyrmion equilibrium energy on the film thickness in a fixed field $H/H_D = 0.4$ is shown.

The results of numerical simulations show that the helicoids also become inhomogeneous in film thickness (see video in [65]). Conical states whose axes are perpendicular to the film are compatible with the film geometry, and free boundary conditions do not impose restrictions on such modulations. For numerical calculations of modulated structures, it is convenient to enter a dimensionless energy density:

$$e = \frac{2\langle E\rangle}{MH_D},$$

where $\langle E\rangle$ is the energy density averaged over the modulation period. Then, according to (5), in the conical phase of the bulk sample,

$$e_{\text{cone}} = -\left(1 + \frac{H^2}{H_D^2}\right).$$

Calculations show that the conical phases of the film and of the bulk sample are almost identical and give the same values of the equilibrium energy density. Conical states (4) exist even in films with a thickness less than the helix period.

The equilibrium energy densities for the helicoidal structure e_{HS} and the 3D skyrmion lattice e_{SL} were calculated. They are compared with the energy density of the conical phase e_{cone}. Figure 8b shows the dependence of the $\Delta e_{\text{HS–cone}} = e_{\text{HS}} - e_{\text{cone}}$ and $\Delta e_{\text{SL–cone}} = e_{\text{SL}} - e_{\text{cone}}$ differences on the magnetic field, together with the corresponding results for the 1D helicoid and the lattice of 2D skyrmions in bulk cubic helimagnets. The functions Δe are constructed for the normalized film thickness values $L/L_D = 0.25$ and 0.5.

In bulk samples, the conical phase has the lowest energy at all values of H less than the saturation field H_D. This situation persists in sufficiently thick films (see inset in Fig. 8a). However, the energy balance between the phases changes dramatically when the film thickness is less than a certain critical value. Then, 3D modulated helicoids and skyrmion lattices become energetically more advantageous than the conical phase (Fig. 8b), meaning that, in sufficiently thin films of a 3D cubic helimagnet, conical modulations of helicoids and skyrmion lattices provide a specific mechanism for stabilizing these structures in a wide range of magnetic fields.

Figure 9a shows the structure of a homogeneous untwisted skyrmion tube in thick films or in bulk samples. Figure 9b schematically shows the result of numerical calculations of the structure of a skyrmion tube in a thin film. This case is characterized by a magnetization twist nonuniform along the thickness of the film. The magnetic moments in the top surface layer are slightly inclined to the center of the skyrmion, while in the lower part of the film, however, they are slightly inclined from the center. Twisting of spins on the top and bottom faces of the film corresponds to intermediate configurations between pure Bloch ($\Phi = \pi/2 + \phi$) and Néel ($\Phi = \phi$) types of skyrmions. Note that the largest deviations are observed for spins near the surface of the film, where they are weakly coupled among themselves due to the smaller number of neighbors. The energy gain from the contribution of the DM interaction accumulates along the film thickness and reduces the overall energy of the state, so that in a certain range of the magnetic field and film thickness a nonuniform skyrmion tube becomes energetically more favorable than the conical phase.

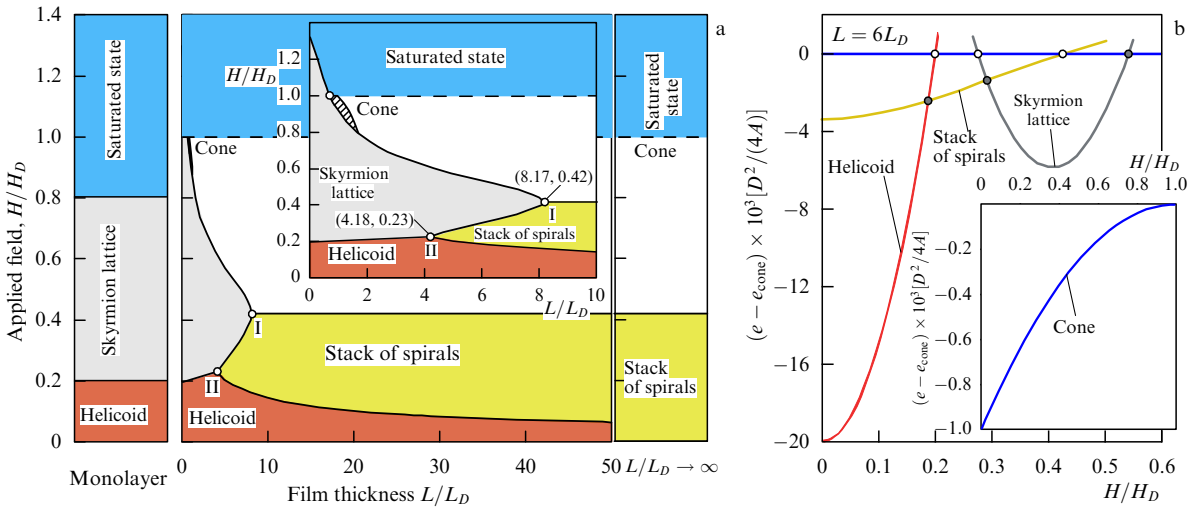

Figure 10. (a) (Color online.) Phase diagram of magnetic states in an isotropic chiral magnet film. (b) Average energy density of different phases depending on the applied magnetic field for the film thickness $L = 6L_D$.

In the first direct observations of chiral skyrmions in the $Fe_{0.5}Co_{0.5}Si$ compound, the film thickness was $L = 20$ nm and $L_D = 90$ nm, which is significantly less than the critical thickness. Thus, the magnetization twist inhomogeneous in the film thickness is the key to elucidating the mechanism of stabilization of 3D skyrmions at low temperatures. The effect of twisting skyrmion tubes was first experimentally detected in [66, 67] and confirmed by subsequent studies (see [68] and references therein).

5. Phase diagram for an isotropic helimagnet film

In Section 4, it was noted that there is a critical thickness of the film at which, when exceeded, the gain in energy from the twisting of the magnetization near the surface of the film becomes insufficient to stabilize the skyrmion lattice. The phase diagram of the film of an isotropic helimagnet is calculated in [69] to determine the ranges of thicknesses and magnetic fields that determine the stability regions of lattice of skyrmions and other states. A comparison of the energy densities of each of the equilibrium states obtained by minimizing the energy functional

$$E = A\,\frac{\partial \mathbf{n}}{\partial x_i}\,\frac{\partial \mathbf{n}}{\partial x_i} + D\mathbf{n}\,\mathrm{rot}\,\mathbf{n} + MH(1 - n_z) + E_0\,, \qquad (15)$$

where E_0 is the energy of the saturated ferromagnetic state, allows us to determine the geometric and material parameters of the film corresponding to different phases.

In the phase diagram shown in Fig. 10a, the thickness of the film and the magnitude of the magnetic field directed normal to the surface of the film are given in dimensionless units L/L_D and H/H_D, respectively. In the central part of Fig. 10a, the film thickness varies from 0 to $50L_D$ (where L_D is the period of the helicoid at $H = 0$). The inset shows details of the phase diagram for films with thickness $0 < L \leqslant 10L_D$. Isolated metastable skyrmions have the lowest energy in the small shaded area of the conical phase. The left part of Fig. 10a corresponds to a monolayer (two-dimensional helimagnet), and the right one corresponds to the case of an extremely thick film (a bulk crystal). Circles I and II with coordinates L/L_D and H/H_D correspond to triple points. Quantities L_D and H_D are expressed in terms of material parameters A, D, M that can be measured experimentally. Solid curves in Fig. 10a correspond to first-order phase transitions among the helical spin spiral (red area), skyrmion lattice (grey), conical phase (white), and new phase (yellow), called stacked spin spirals (SSSs). The horizontal dashed line indicates a second-order phase transition between the conical phase and the saturated ferromagnetic state (blue area).

In contrast to the phase diagram proposed in [70], the phase diagram shown in Fig. 10a contains five phases and two triple points. The triple point I determines the critical thickness of the film $L^* = 8.17L_D$, beyond which skyrmions can only exist in a metastable state. For example, for MnSi ($L_D = 18$ nm) and FeGe ($L_D = 70$ nm), the critical values are $L^* = 150$ nm and $L^* = 570$ nm, respectively. As the film thickness decreases, the interval of magnetic fields in which the skyrmion lattice is formed increases. This fact reflects an increase in the relative contribution of surface twists with a decrease in thickness. There is another critical point at which, at $L < 0.68L_D$, the conical phase is completely suppressed and becomes energetically unprofitable over the entire range of fields.

It is important to note that the chiral surface twists discussed in Section 4 also add additional modulation to the helicoidal spiral state. The vector $\mathbf{k}$ of such a helix lies in the film plane orthogonal to the applied field. Surface-induced modulations reduce the energy of the helix and, in a certain range of fields, make it energetically more advantageous than the conical state. The distribution of magnetization in a thin film is very different from that in bulk cubic chiral crystals, where any small magnetic field leads to the transformation of the helix into a conical phase, or rather into the SSS, according to the results presented in the right part of Fig. 10a.

Note that the surface twist effect is not limited to the surface of the film, but also appears on the side faces of the sample. We emphasize that the continual 3D model of an isotropic chiral magnet is not reduced to a simple 2D model in the other limiting case, when $L/L_D \to 0$. This is illustrated in the left part of Fig. 10a, where a 2D phase diagram is given for a single isotropic monolayer or for a multilayer structure with an interface induced by the DM interaction of certain crystal symmetries, e.g., C_{nv}, D_{2d}, and S_4 [13, 64]. Figure 10b shows the dependence of the average energy density of different phases on the applied magnetic field for a film of thickness

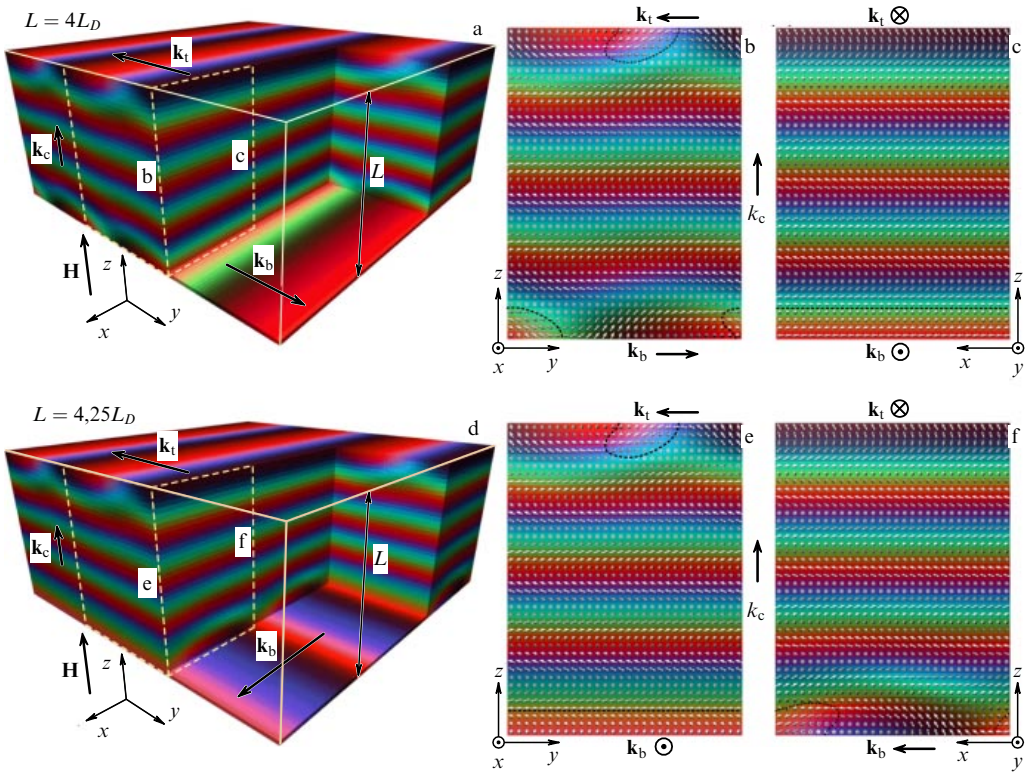

Figure 11. (Color online.) Stacks of spin spirals. Local directions of magnetization in the film are indicated by color in accordance with the scale shown in Fig. 7.

$L = 6L_D$. The inset in this figure shows the dependence of the energy of the conical phase on the applied field.

A wide range of the phase diagram is occupied by the SSS area. Triple point II determines the thickness limit of the film, beyond which SSSs can appear as the global minimum energy of the system. Figure 11 illustrates the complex spin structure of SSSs.

The spin structure of SSSs represents the interference of the conical phase in a sample volume with quasi-helical magnetization modulation localized near its surface. Such surface modulations have a finite depth of penetration and appear on the upper and lower surfaces. They have a mixed helical ($\theta = \theta(y)$, $\Phi = \pi/2$) and cycloidal ($\theta = \theta(y), \Phi = 0$) modulation type. The period of surface helical modulations is always longer than that of ordinary helicoids (6), and it increases with increasing field.

Figure 11a shows the distribution of magnetization in a film with thickness $L = 4L_D$. Vector $\mathbf{k}_c$ indicates the direction of propagation of the conical helix in the film volume, and vectors $\mathbf{k}_t$ and $\mathbf{k}_b$ indicate the direction of propagation of complex spin helices on the upper and lower surfaces of the film, respectively. At this film thickness, the vectors $\mathbf{k}_t$ and $\mathbf{k}_b$ are counter-directed and orthogonal to the vector $\mathbf{k}_c$.

Figures 11b, c show the magnetization distributions in the film cross sections by yz and xz planes (these cross sections are highlighted by dashed rectangles in Fig. 11a). Figures 11c–f illustrate the distribution of magnetization in a film of thickness $L = 4.25L_D$. For such a film, the equilibrium stack of helices is characterized by mutually orthogonal vectors $\mathbf{k}_t$, $\mathbf{k}_b$, and $\mathbf{k}_c$. The black dashed curves in Fig. 11b, c, e, f highlight small volumes near the surface of the film with a negative magnetization projection, $n_z < 0$. The relative orientation of the spin helix vectors on the upper and lower surfaces, $\mathbf{k}_t$ and $\mathbf{k}_b$, respectively, depends on the thickness of the film. The angle β_{tb} between $\mathbf{k}_t$ and $\mathbf{k}_b$ for the SSS equilibrium phase varies depending on the film thickness. In particular, when the $L = (n + 1/2)L_D$ condition is met (n is an integer), the equilibrium values of β_{tb} are zero and gradually change depending on the thickness: $\beta_{tb} = 90^\circ$ at $L = (n + 3/4)L_D$, $\beta_{tb} = 180^\circ$ at $L = (n + 1)L_D$, and $\beta_{tb} = 90^\circ$ at $L = (n + 5/4)L_D$.

Due to the relatively weak dependence of the energy of thick films on the angle β_{tb}, in such samples we should expect a strong influence of crystallographic anisotropy on the mutual orientation of the vectors $\mathbf{k}_t$ and $\mathbf{k}_b$.

Model (15) does not take into account the surface properties of real samples, which depend on surface doping, modifications of the crystal structure, the formation of terraces, etc. All this changes the electronic spectrum of the surface layers of the medium, and therefore the parameters of the model. Due to changes in the constants of the exchange and spin-orbit interactions, we can expect a slight modification of the absolute values for the observed quantities, phase transition lines, and critical points on the phase diagram. At the same time, the contribution of surface effects in the first approximation must be proportional to the ratio λ/L_D of thickness λ of such a surface layer to the penetration depth L_D of surface spin modulations (SSMs). Usually, λ is of the order of several interatomic distances a, while for helimagnets L_D is of the order of several tens or hundred a. Therefore, in chiral magnets with long-period structures, the contribution of surface atomic layers with changed parameters is negligible compared to the contribution of SSMs.

6. Chiral bobber

A rich variety of metastable states is inherent in many fields of modern physics. Particular attention is drawn to states

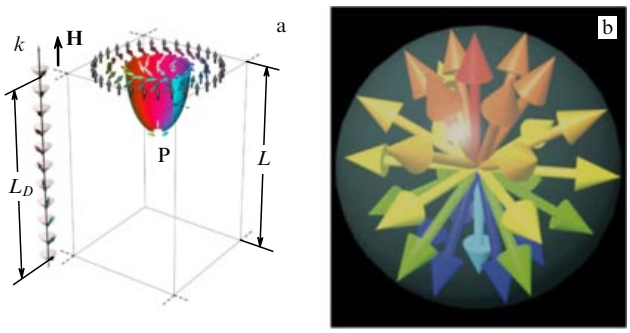

Figure 12. (Color online.) Schematic representation of the vector field **n** for (a) a chiral bobber in the conical phase and (b) the Bloch point.

characterized by a high energy barrier that can remain metastable for a long time. Such states are of particular interest for optical, magnetic, and electronic information storage technologies. In principle, all modern electronics and spintronics are based on working with and managing such metastable states. In particular, magnetic domains in magnetic storage devices are the best examples of metastable states separated by high-energy barriers. High-energy barriers in hard drives are created due to the strong crystallographic anisotropy of the material, which attaches magnetic domains to their positions. The disadvantage of such data storage is that the detector must be moved to the location where the data bit is contained, or the entire data carrier must be moved in the direction of the detector.

Modern spintronics offers many alternative ideas for a new generation of magnetic data storage devices that are based on the use of mobile metastable states. The most interesting candidates are domain walls in nanostrips [71] and magnetic chiral skyrmions (CSs) [64, 72, 73]. Chiral vortices of these types are considered promising particles in the field of information technology due to their unusual transport properties, as well as their compact size, which under certain conditions can be reduced to several nanometers [74] or even to several atomic distances [75]. In addition, this is an interesting and important topic of fundamental research for nonlinear physics.

In [32], a new type of particle-like state in chiral magnets was predicted, which was named the 'chiral bobber' (CB) by the authors of the article. Such a quasiparticle in a wide range of parameters turns out to be more compact than a chiral magnetic skyrmion, and is more energy efficient. A CB is a three-dimensional localized finite-energy soliton in nonlinear field equations, consisting of a smooth vector field of magnetization and a 'hedgehog' type magnetic singularity (Fig. 12). Unlike previously known magnetic localized structures (domain walls, helices, skyrmions, vortices), a thermodynamically stable CB is formed at the phase interface or on the surfaces of chiral magnets. Next, we present the main results of Ref. [32].

For numerical calculations of the chiral bobber in [32], the energy density on a discrete lattice was used, which includes the Heisenberg exchange coupling, the DM interaction, and the Zeeman interaction:

$$E = -J\sum_{\langle ij\rangle} \mathbf{n}_i\mathbf{n}_j - \sum_{\langle ij\rangle} \mathbf{D}_{ij}[\mathbf{n}_i \times \mathbf{n}_j] - \mu_s \mathbf{H}\sum_i \mathbf{n}_i\,. \qquad (16)$$

Here, the symbol $\langle ij\rangle$ denotes the summation over pairs of nearest neighbors, $\mathbf{n}_i = \mathbf{M}_i/\mu_s$ is a normalized unit vector of the magnetic moment on the ith node of the lattice, J is a constant of exchange interaction, $\mathbf{D}_{ij}$ is a Dzyaloshinskii–Moriya vector, $\mathbf{D}_{ij} = D\mathbf{r}_{ij}$, where D is a scalar, the unit vector $\mathbf{r}_{ij}$ is directed from node i to node j, and $\mathbf{H}$ is an external magnetic field applied along the z axis perpendicular to the film plane. To preserve the generality of the results of a discrete model and the possibility of comparing them with the conclusions of the continuum model, we use the previous notation for the parameters L_D and H_D:

$$L_D = 4\pi\,\frac{A}{D} = 2\pi a\,\frac{J}{D}\,, \qquad H_D = \frac{D^2}{2MA} = \frac{D^2}{\mu_s J}\,,$$

where a is the lattice constant.

Direct minimization of Hamiltonian (16) was performed using the nonlinear conjugate gradient method with adaptive stereographic projections based on the CUDA architecture [63].

Everywhere inside the conical phase in Fig. 11a (except for the shaded area), a new structure (CB structure) , which is a truncated 3D skyrmion, corresponds to the metastable state with the lowest energy (Fig. 12a). The vector field of such a structure is characterized by an almost parabolic isosurface $n_z = 0$ and a topological singularity at the point P, which is located inside the film at a finite distance r_P from the surface. This type of singularity is known in ^{3}He as a hedgehog [8], and in ferromagnets as a Bloch point [10] (Fig. 12b). In the case of other condensed matter, such as ultra-cold gas [76] and spin ice [77], it is called a magnetic monopole.

Hedgehog structure

$$\mathbf{n} = \frac{\mathbf{r}}{|\mathbf{r}|}$$

can be obtained explicitly from the Hamiltonian (15) equations in the zero magnetic field. The magnetic field deforms the magnetization field, and the hedgehog transforms into a chiral Bloch point. In the $z = \text{const}$ plane cross section, the CB spin structure simulates a field of 2D skyrmions whose diameter decreases with increasing distance from the film surface. The depth of penetration into the film satisfies the condition $r_P \leqslant L_D/2$ with an accuracy of $\pm a/2$. In view of the significant chirality of the state and its localization near the surface of the film, like a bobber on the surface of water, the structure under consideration was called 'bobber'. Visualization of the CS and CB spin structure is given in [78] (videos 1 and 2).

Note that the possibility of such topological defects has been discussed in the context of various physical problems. "A vortex with an end is an unexpected phenomenon" [79]. An analog of the bobber in an unlimited A-phase of an ^{3}He environment was first discussed in [80–82]. Such structures — solitons ending with a hedgehog of the field **d**, called Dirac monopoles — were observed in Bose–Einstein condensate [76, 83]. In [76], the inhomogeneous rotation of the spins of ultracold rubidium atoms under adiabatic changes in the magnetic field induced the flow of a superfluid liquid at the velocity of **v**. The vorticity $\boldsymbol{\omega} = \mathrm{rot}\,\mathbf{v}$ of the velocity field corresponded to a semi-infinite vortex line (a Dirac string). The end point of this line gives the magnetic field of the monopole $\mathbf{B} \sim \mathbf{r}/r^3$. Finally, in [84], the formation of 2D vortices from truncated 1D domain walls was studied, and the formation of a soliton from a vortex with a half-integer quantum in the A-phase of ^{3}He was described in detail in monograph [8].

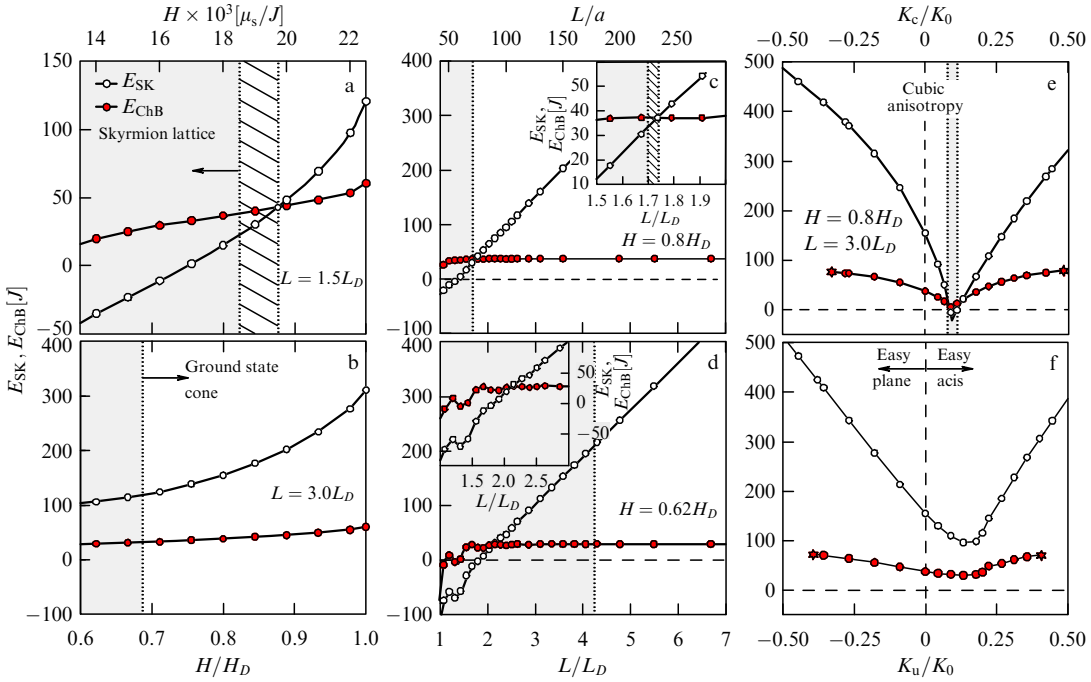

Figure 13. (Color online.) Dependences of the energies for an isolated CS (white dots) and CB (red dots) on the magnetic field at a fixed film thickness (a, b) and on the film thickness at a fixed field (c, d). The dependences of CS and CB energies on the parameters of cubic (e) and uniaxial (f) anisotropy in fixed values of film thickness and magnetic field.

The dependences of the CS and CB energies on the external magnetic field and the sample thickness are shown in Fig. 13. The CS and CB energies are reckoned from the energy of the conical phase. Figures 13a–d correspond to the isotropic case, i.e., the uniaxial (K_u) and cubic (K_c) anisotropy constants that can be induced by interfaces or external stresses are zero here, $K_c = K_u = 0$. Parameter values used in the calculations: $J = 1$, $D = 0.15$ ($L_D = 41.89a$). The simulated area contained $56 \times 256 \times Ln$ spins, where $Ln = 40-280$. White and gray areas in Fig. 13a–d represent the stability regions of the conical phase and of the skyrmion lattice, respectively, and in the dashed region of the conical phase, the CS energy is less than the CB energy. As can be seen from these figures, almost everywhere within the conical phase, the CB has an energy much smaller than the CS. The difference between the CS and CB energies becomes more pronounced when the film thickness changes (Fig. 13c, d). The CS energy increases linearly with increasing film thickness. At the same time, due to the localization of the CB near the surface, its energy is almost independent of the film thickness. This regularity is broken only in small fields and for very thin films outside the stability region of the conical phase (see insets in Fig. 13c, d).

In [32], the anisotropy energy was added to the energy (16) to evaluate the stability of CBs in anisotropic crystals E_a:

$$E_a = -\sum_i \left[K_u n_{i,z}^2 + K_c \left(n_{i,x}^4 + n_{i,y}^4 + n_{i,z}^4 \right) \right],$$

where $n_{i,\alpha}$ ($\alpha = x, y, z$) is an α-component of the unit vector **n** on the node i.

Figures 13e, f show the dependence of the CS and CB energy on the anisotropy constants for fixed external field $H = 0.8H_D$ and film thickness; the anisotropy constants are given in units $K_0 = D^2/(2J)$. According to these results, within the conical phase, the CB is always more energy efficient than the CS. The asterisks in Fig. 13e, f correspond to the points of collapse of the CB. Due to the presence of free boundaries, the CB topology must be described in terms of relative homotopy groups [85]. The corresponding group $\pi_2(S^2, S^2) = 0$ is trivial. This means that the geometric singularity of the CB field can be displaced to the surface and then smoothed out. Despite this, the chiral bobber has a high energy barrier. To estimate it, the minimum energy path was calculated using the Geodesic Nudged Elastic Band method (GNEB) [86]. It is shown that the energy barriers for CSs and CBs have a comparable height. Based on this, we can conclude that the thermal stability range for CBs will have the same order of magnitude as for isolated CSs. In addition, due to the high activation energy, it can be expected that the probability of spontaneous generation of a CS by thermal fluctuations is significantly less than that for a CB. This conclusion is confirmed by the results of Monte Carlo simulation. With parameters $L = 2.36L_D$ and $H = 0.8H_D$, the spontaneous initiation of a CB is observed during simulated annealing, while a CS does not occur in this mode [78].

7. Experimental observation of a chiral bobber in thin films of a FeGe helimagnet

Chiral bobbers were experimentally detected [87] in thin films of FeGe helimagnet using off-axis electronic holography (EH). The EH method is based on the Aaronov–Bohm effect [88]: in quantum mechanics, the interaction of a charged particle with an electromagnetic field is not reduced to the local influence of the Lorentz force on it. EH provides quantitative measurement with high spatial resolution of the phase ϕ_M of an incident electron beam interacting with magnetic induction components inside and outside the sample [89]. The wave function of the incident electron beam interferes with the reference electron wave whose phase ϕ_0 is known. In the interference pattern, the intensity

distribution I has the form

$$I = A_1^2 + A_2^2 + 2A_1A_2\cos(\delta\phi),$$

where A_i ($i = 1, 2$) are wave amplitudes, and $\delta\phi = \phi_M - \phi_0$ is the difference between their phases.

In the quantum-mechanical description of an electron, the Schrödinger equation includes the vector potential $\mathbf{A}$, not the magnetic field $\mathbf{B} = \mathrm{rot}\,\mathbf{A}$. In particular, the wave function of a beam of electrons moving along the z axis in the vector potential field $\mathbf{A}$ acquires the phase

$$\phi(x, y) = -\frac{2\pi e}{h}\int A_z(x, y, z)\,\mathrm{d}z\,. \tag{17}$$

In the EH method, the change in the phase $\delta\phi$ of the wave function of the incident electrons is proportional to the magnetic flux Φ_M through the contour D, which is formed by parallel electron trajectories of the incident and the reference beams closed at infinity:

$$\delta\phi = -\frac{2\pi e}{h}\oint_D \mathbf{A}\,\mathrm{d}\mathbf{l} = -\frac{2\pi e}{h}\,\Phi_M(S)\,.$$

Here, S is the area bounded by the contour D, $2\pi e/h$ is the quantum of the magnetic flux. Relation (17) for the change in the phase of the wave function of the electron beam with the change in the values of the vector potential in spatial domains where there is no magnetic field expresses the Aaronov–Bohm effect [88].

The vector potential is determined by the dipole–dipole interaction and depends on the magnetization distribution in the sample volume V_0:

$$\mathbf{A}(\mathbf{r}) = -\frac{\mu_0}{4\pi}\int_{V_0}\mathbf{M}(\mathbf{r}')\times\frac{\mathbf{r}-\mathbf{r}'}{|\mathbf{r}-\mathbf{r}'|^3}\,\mathrm{d}\mathbf{r}'\,. \tag{18}$$

According to (17) and (18), the contribution of magnetization to the phase shift is as follows:

$$\phi_M = -\frac{\mu_0 e}{h} \times\int\frac{(y-y')M_x(x', y') - (x-x')M_y(x', y')}{(x-x')^2 + (y-y')^2}\,\mathrm{d}x'\,\mathrm{d}y', \tag{19}$$

where M_x and M_y are the magnetization components averaged over the film thickness,

$$M_i(x', y') = \int M_i(\mathbf{r}')\,\mathrm{d}z', \qquad i = x, y\,.$$

In [87], experimental observations were supplemented with micromagnetic calculations in the framework of the model of a helimagnet with energy density

$$W = A\,\frac{\partial\mathbf{n}}{\partial x_i}\,\frac{\partial\mathbf{n}}{\partial x_i} + D\mathbf{n}\,\mathrm{rot}\,\mathbf{n} - M\mathbf{B}_{ext}\mathbf{n} - \frac{1}{2}\,M\mathbf{B}_d\mathbf{n}\,. \tag{20}$$

Here, $\mathbf{B}_{ext}$ is the external magnetic field, and $\mathbf{B}_d$ is the magnetostatic field of the sample. Since CB, unlike CS, has a finite penetration depth and occupies a much smaller volume, the phase shift (19) caused by the CB must be weaker than that caused by the CS. This assumption is confirmed by the results of micromagnetic simulation.

A quantitative comparison of the measured and theoretically calculated phase shift makes it possible to identify CBs and CSs and distinguish them. Most EH measurements were performed on three FeGe samples.

Following the theoretical predictions of spontaneous generation of CBs under the conditions of film annealing in a magnetic field, the authors of [87] performed EH experiments with cooling samples from high to low temperature in a constant magnetic field $\mathbf{B}_{ext} \parallel \mathbf{e}_z$. Most of the EH measurements were performed on three FeGe samples of different shapes.

Here, we present experimental data for sample S1, which is a nanostrip with varying thickness (Fig. 14a). Figure 14b shows typical phase shift images and corresponding profiles obtained after cooling the sample from a temperature of $T_{ext} = 240$ K to $T = 95$ K at $B_{ext} = 200$ mT, followed by increasing the field B_{ext} to 300 mT. Figure 14b shows an image of the portion of the sample highlighted with a dashed line in Fig. 14a. The phase shift of images mainly demonstrates a contrast characteristic of magnetic skyrmions, i.e., bright spots with a bell-shaped profile with almost identical intensities and sizes (Fig. 14b). The change in the phase shift along the strip for skyrmions (blue line) and bobbers (red line) is shown in Fig. 14c. As can be seen, there is a linear increase in the phase shift of a signal from the CS chain along the film thickness gradient (dashed line in Fig. 14c). However, a quantitative analysis of the phase shift profiles revealed the presence of two different objects with different intensities and values of φ. Objects with a weaker contrast marked in Fig. 14b with red arrows correspond to CBs observed in the micromagnetic simulation. In a wedge-shaped sample, such objects appear only in films with thicknesses exceeding the critical value (at $L \geqslant 110\ \mathrm{nm} \approx 1.6L_D$). The position, size, and intensity of these objects depend on the magnitude of the magnetic field. The theoretical dependence φ on the magnetic field is consistent with experimental data.

Objects of low intensity are identified with CBs, because their properties are consistent with theoretical predictions. However, the spontaneous generation of CBs during annealing in the field corresponds to a metastable state and is a rare event. In most cases, this procedure leads to a pure multiskyrmion state.

To systematically study CBs, we managed to find a reliable way to generate them. In the course of micromagnetic modeling, the generation of CBs was revealed from a defect in the helicoidal structure of the type of edge dislocation with a small inclination of the external magnetic field. With an increase in the field, the helicoidal isosurfaces demonstrate a slope of helix vector $\mathbf{k}$ to the direction of the vector $\mathbf{B}_{ext}$. At a certain value of the field, a fold is formed on the isosurface, which in turn leads to the appearance of a Bloch point near the surface of the sample, which then penetrates from the surface into its volume to a certain depth. This state remains stable only within a narrow range of fields and becomes a CB when the magnetic field increases further. By a similar mechanism, Bloch points appear in the skyrmion lattice and in the helical phase [90, 91].

In an experimental setup, the direction of the applied field is always fixed and coincides with the direction of the incident electron beam. The slope of the field is reached by turning the sample around two mutually orthogonal axes, so that the vector $\mathbf{B}_{ext}$ forms an angle of 10° with the normal to the plate. The obtained multiple images of the phase shift in all samples illustrate:

(1) a weaker contrast of CBs than that of CSs;

(2) the reproducibility of a CB in an oblique field;

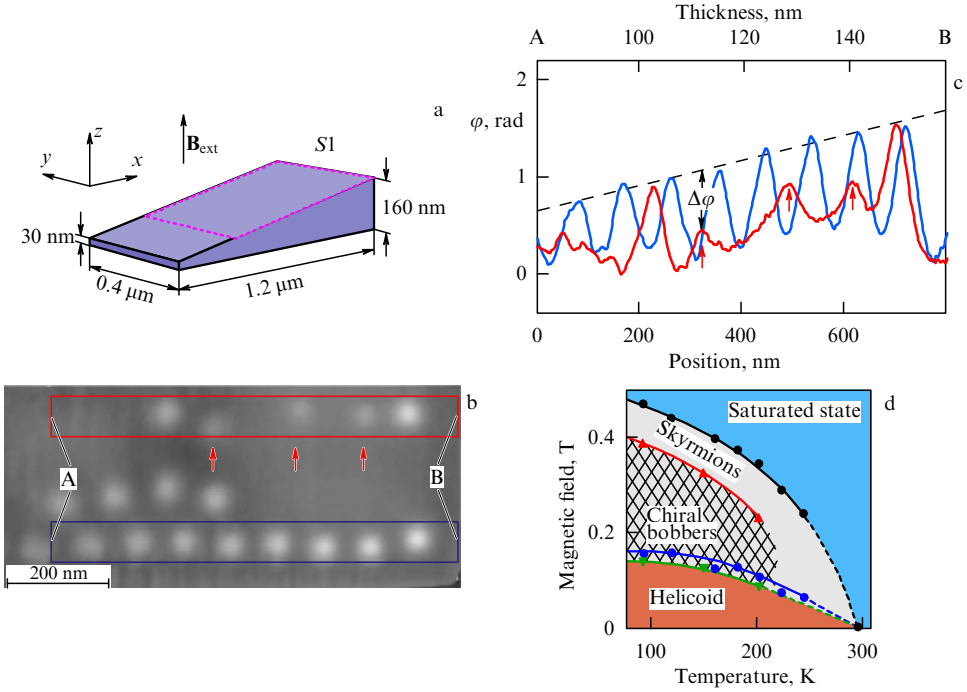

Figure 14. (Color online.) Experimental proof of the origin of magnetic bobbers under the conditions of annealing samples in a magnetic field (see explanations in the text).

(3) the appearance of CBs in different positions in the sample;

(4) CB mobility in the applied field;

(5) quantitative agreement of the measured value of the phase shift with the theoretical one.

A reliable method for generating CBs also allowed us to study their stability with increasing temperature. Figure 14d shows a phase diagram in the magnetic field–temperature variables based on a large number of experimental data. The gray area corresponds to the stability range of magnetic skyrmions. This area is bounded by the collapse field (black line) and the elliptical instability field (green line). The blue line corresponds to the origin of the CS (the transition from a helicoidal structure to isolated skyrmions as the field increases). Note that the elliptic instability fields are smaller than the CS generation fields. The shaded part of the gray area corresponds to the CB area of existence. This region is bounded at the bottom by the same elliptical instability field, but has much lower collapse fields than for CSs. The red line shows the temperature dependence of the CB collapse field.

The equilibrium distance between the CB (CS) and the edge of the sample increases with increasing field and shows the same character of Lennard-Jones type interaction found for CSs [92].

Experimental evidence of the formation of chiral bobbers is presented independently in [93] by measuring the susceptibility in FeGe/Si thin films (111). It is shown that the CB predicted in [87] as a metastable state is stable in the presence of additional Dzyaloshinskii–Moriya–Rashba interfacial interactions. The results of the magnetization measurements presented in [93] are interpreted as proof of the formation of a lattice of chiral bobbers at the FeGe/Si interface.

A chiral skyrmion, in addition to being of academic interest, shows prospects for practical applications. For more than half a century, hard disk drives have been the main storage devices of digital data. Currently, they have high reliability and are widely used. However, the density of recording information on magnetic drives and the speed of their operation are limited by thermal effects [94]. In addition, the complexity and fragility of the mechanical parts of magnetic drives are motivating the search for new solid-state devices with comparable or higher bit densities. In recent years, alternative solid-state magnetic memory devices without moving mechanical parts have been proposed. The most promising of them are based on the concept of racetrack memory [71]. In this case, the role of information carriers is played by: (1) magnetic domain walls in nanowires — narrow transition layers between regions with opposite directions of magnetization [71] or (2) chiral skyrmions in a magnetic nanotape [64].

CSs are topologically stable and can be moved by currents that are several orders of magnitude lower than those required to move domain walls [72]. Stack memory on skyrmions is currently considered the most efficient. However, the use of CSs only for coding data involves 'quantization' of the distances between skyrmions on the racetrack. In addition, CSs are highly mobile and interacting objects, and thermal fluctuations cause them to drift. These factors make it difficult to maintain the distance between CSs along the track. To solve this problem, [73] proposes a special design in which skyrmions can move along parallel nanostrips. For thermal fluctuations, a CS does not change its strip, since different strips are separated from each other by high energy barriers.

Section 6 shows that the energy barriers that protect skyrmions and bobbers are of the same order of magnitude, and these two objects are possible candidates for use as carriers of bits 1 and 0. In [87], a binary data stream representing a sequence of ones and zeros is proposed to be encoded using a sequence of movable skyrmions and bobbers of two types. With this approach, there is no need to maintain a certain distance between carriers. The coherent motion of

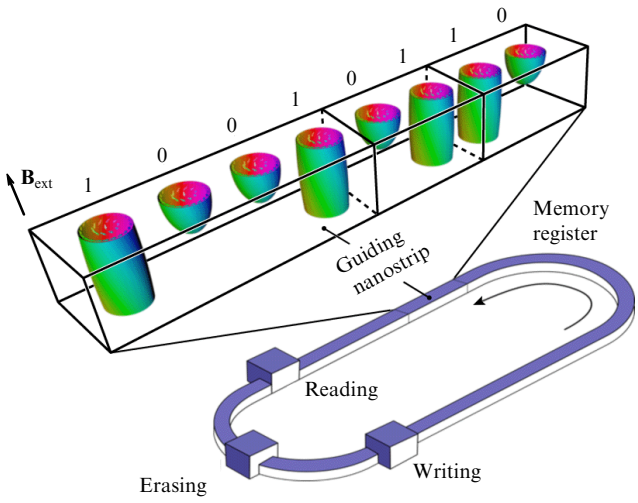

Figure 15. (Color online.) An alternative concept of magnetic solid-state memory based on encoding the data stream in nanostrips with skyrmions and bobbers.

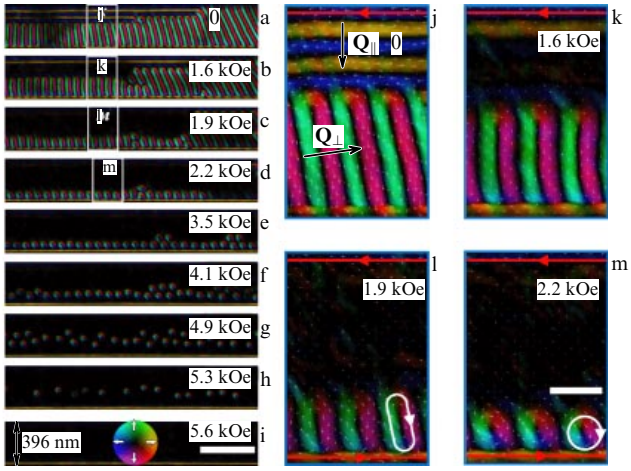

Figure 16. (Color online.) Evolution of spin helicoids when the magnetic field changes in an FeGe nanostrip with a width of 396 nm at $T = 100$ K.

CBs and CSs is expected to be stable due to the coupling force in interparticle interactions. A conceptual diagram of a single register in such a storage device is shown in Fig. 15.

A nanostrip has the form of a closed track and contains a chain of alternating magnetic skyrmions and chiral bobbers that play the role of bits 1 and 0. Writing, reading, and erasing information are performed on different parts of the guiding track. Spin structures for CSs and CBs in Fig. 15 are schematically represented by their isosurfaces.

8. Interaction of skyrmions

Studies of the mechanisms of skyrmion formation, scenarios of their evolution in crystals of limited geometry (nanowires and nanostrips), and the interaction of skyrmions with each other and with the edges of samples are important not only for possible technological applications but also for the further development of fundamental research.

The transformation of the helicoidal ground state of an FeGe nanostrip into individual skyrmions and skyrmion chains in the magnetic field, as well as the interaction of skyrmions with the edges of the sample, was experimentally observed in [95], where the dynamics of magnetization in strips with width $w = 396$ nm at temperature $T = 100$ K was systematically studied.

Figures 16a–i illustrate the evolution of spin textures with increasing magnetic field. The corresponding enlarged images are selectively shown in Figs 16j–m. In the absence of a field, an almost helicoidal structure was observed in a strip $w = 130$ nm wide.

Figures 16a, j show that at width $w = 396$ nm, a helicoidal state occurs in the strip with the coexistence of two helices: (1) with a wave vector $\mathbf{Q}_\parallel$ parallel to the edge of the strip (an ideal helical structure) and (2) with a wave vector $\mathbf{Q}_\perp$ orthogonal to edge (a distorted edge helical structure). When a magnetic field $\mathbf{B}$ is applied perpendicular to the nanostrip plane, these helices change in different ways. In field $B \sim 1.6$ kOe (Fig. 16b, k), the helices with $\mathbf{Q}_\perp$ become less noticeable, while the helices with $\mathbf{Q}_\parallel$ begin to deform. When the magnetic field reaches the value $B = 1.9$ kOe, the helices with $\mathbf{Q}_\perp$ completely disappear, and the helices with $\mathbf{Q}_\parallel$ transform into a structure of strips of finite length (bimerons) (Fig. 16c, l). As the field increases further, the strip structure transforms into a chain of skyrmions stretched along one of the edges of the nanostrip (Fig. 16d, m). This fact indicates that skyrmions can only be created from helices with a distorted structure along the edge of the nanostrip.

The high mobility of skyrmions in a magnetic field demonstrates itself in their unfixed positions. For example, as seen in Fig. 16d, in the field $B = 2.2$ kOe, the chain of skyrmions near the upper right edge of the strip merges with the one near the lower edge of the strip when the field is increased to $B = 3.5$ kOe (Fig. 16e) without the birth of new skyrmions or the destruction of the former ones. Similar phenomena are also found in nanostrips with different widths.

Despite the high mobility of skyrmions, the equality of the number of periods of the helix and the number of skyrmions formed from it is always maintained. After a chain of skyrmions has been formed along the edge of the nanostrip (Fig. 16g), a further increase in the magnetic field leads to the movement of this chain into the inner region of the strip (Fig. 16d–g). At the same time, the number of skyrmions remains unchanged in a wide range of magnetic fields ($2.2 < B < 4.9$ kOe). Conservation of the number of skyrmions is related to their topological stability. The collective motion of skyrmions is due to the *repulsion at small distances of edge spins and skyrmions*. With a further increase in the field, the skyrmion chain is distorted (Fig. 16g), the skyrmions in it gradually disappear (Fig. 16h), and in fields $B > 5.3$ kOe, a transition of the system to a homogeneous ferromagnetic state is observed (Fig. 16i). Red arrows indicate the orientation of the magnetization near the edges of the strip.

The nontrivial interaction of skyrmions in the conical phase was first discovered in [92] using numerical modeling in the framework of the standard model of a helimagnet (15). Numerical calculations of the structure of skyrmions in the field $H = 0.57H_{\text{d}}$ and analysis of their interaction in thin films with thickness L_D were performed. In a cylindrical coordinate system $\mathbf{r} = (\rho\cos\phi, \rho\sin\phi, z)$, the radial energy density

$$e(\rho) = \int_0^{L_D} \mathrm{d}z \int_0^{2\pi} \mathrm{d}\phi\, w(\rho, \phi, z)$$

for a three-dimensional skyrmion with exponentially decreasing asymptotic behavior is negative in the peripheral region of the conical phase. The dependence of the interaction energy of two asymmetric skyrmions $E_{27}(r)$ on the distance between them for different values of the applied magnetic field has the form of a Lennard-Jones type potential and indicates an *attractive* interskyrmion interaction, which is characterized by a low potential barrier and a fairly deep potential energy well for the transition of skyrmions to the bound state (biskyrmion). The nature of this interaction differs from that of skyrmions in the ferromagnetic phase [15, 96], where CSs homogeneous along the z axis in (11) and (12) always repel each other.

Detailed experimental and theoretical studies of the nature of the interaction of skyrmions with each other and with the boundaries of sample in the nanostrips of FeGe chiral magnet were carried out in [97]. It was shown that when the magnetic field exceeds a certain critical value, the nature of interaction between skyrmions changes from attraction to repulsion. Experimentally found field dependences of equilibrium distances between two skyrmions, as well as the distances between an individual skyrmion and the edge of the strip, are quantitatively consistent with the results of micromagnetic simulation.

The authors of [97] managed to go beyond collective phenomena and studied isolated pairs of skyrmions in order to identify the true nature of skyrmion interaction. In addition, an adequate theoretical model of skyrmion interactions, which must be in quantitative agreement with experimental data, requires correct consideration of the dipole–dipole interaction that is always present in the nanostrip. The important role of such interactions which were not taken into account in earlier micromagnetic models is noted in [98], where it is shown that the dipole–dipole interaction significantly affects the equilibrium distances in the skyrmion lattice.

Here are some results of Ref. [97], revealing details of interskyrmion and skyrmion-edge interactions. Figure 17 shows the evolution of two pairs of skyrmions in an FeGe nanostrip (width 430 nm, length 1590 nm, and thickness 120 nm) when the magnetic field $B_{\text{ext}} = \mu H$ increases (Fig. 17a–f) and decreases (Fig. 17g–l). In the experiment, the dependences of equilibrium skyrmion–skyrmion and skyrmion–edge distances on the magnetic field were measured, and the critical field B_{ext} was found for which, if exceeded, skyrmions begin to weakly repel each other. The initial state with a small number of CSs was set by controlling the number of helicoids in the nanostrip. Figure 17a shows that, in the field $B_{\text{ext}} = 255$ mT, two pairs of skyrmions are located near the opposite edges of the sample at a great distance from each other, so the interaction between them can be disregarded. When the field is increased to 400 mT, the smallest skyrmion-skyrmion distance d_{ss} remains almost unchanged (Fig. 17a–d), then in the range from 400 mT to 500 mT it increases sharply (Fig. 17e, f). Unlike d_{ss}, in small fields B_{ext}, the distance from skyrmions to the edges of the strip d_{se} gradually increases (Fig. 17a–c). In fields above 350 mT, they begin to increase dramatically. In stronger fields, $B_{\text{ext}} \sim 500$ mT, skyrmions are concentrated in the middle part of the sample. With a further increase in the field, the skyrmions change their positions slightly, until a collapse occurs. The observed behavior clearly shows that, as the field increases, the interactions among skyrmions change from strong attraction to weak repulsion. A detailed picture of the movement of skyrmions in a magnetic field, in particular their jumps, is given by the animation presented on the websites [99, 100].

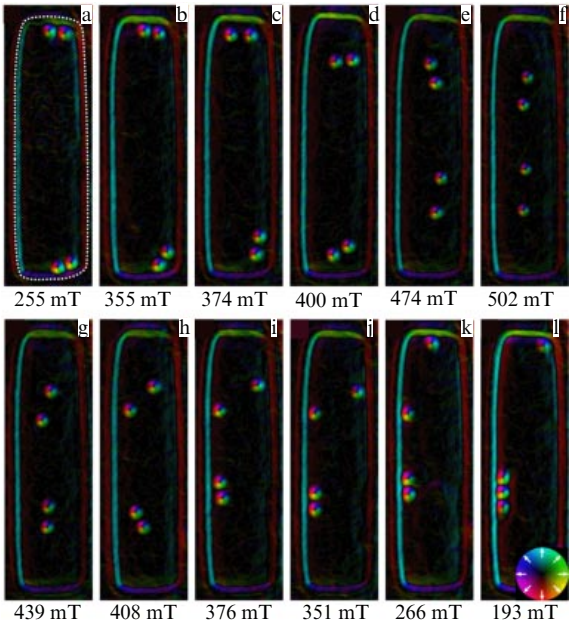

Figure 17. (Color online.) Evolution of a pair of skyrmions when the magnetic field changes in the FeGe plate. The directions of magnetization in the plane are indicated by color.

Full reversibility of states is an important feature of the interaction of skyrmions in a magnetic field. With a decrease in B_{ext} to 408 mT (Fig. 17h), the interskyrmion distance d_{ss} of the lower pair is significantly reduced, which indicates that the attraction between skyrmions is restored. Interestingly, the distance between the skyrmions in the upper pair remains unchanged due to the attraction of skyrmions to the edge of the sample. When the field is further decreased, all skyrmions move to the edges of the strip, where they form pairs or remain isolated (Fig. 17i–k).

Note the relatively large distance between a single CS and a pair of CSs on the left side of the sample at 266 mT (Fig. 17k). These three skyrmions, despite the extremely large distance between them, form a chain when the magnetic field is further decreased to 193 mT (Fig. 17l). Therefore, CSs can be attracted to each other at distances significantly greater than the L_D size of each of them.

Micromagnetic modeling revealed a nontrivial three-dimensional structure of the bound CS pair and the isolated skyrmion. The isosurfaces $\theta = 90^\circ$ and $\theta = 5^\circ$ for them, represented by closed curves, are shown in Fig. 18a, b, and the magnetization distributions in the plane $z = \text{const}$ are shown in Fig. 18c, d. Black and white areas correspond to the values $n_z = 1$ ($\theta = 0$) and $n_z = -1$ ($\theta = 180^\circ$).

Attraction can be explained qualitatively in terms of magnetic poles. The skyrmion in the conical phase consists of the core (the black area in Fig. 18c) with positive energy, where $\theta \approx 0$ (north pole), the shell (white area) with negative energy, where $\theta \approx \pi$ (south pole), and the conical phase (blue area). In the ferromagnetic phase, the structure of skyrmions is quasi-two-dimensional, and they always repel when approaching due to the repulsion of the similar (south) poles. In the conical phase, the structure of a pair of

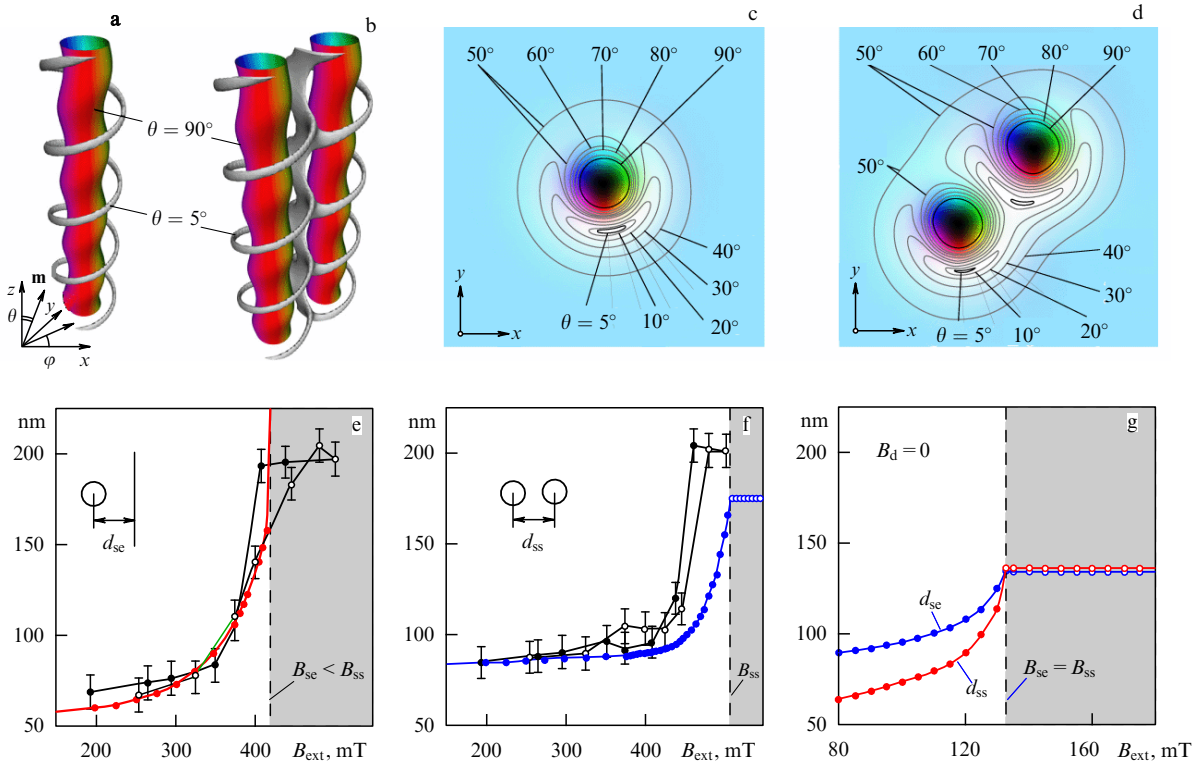

Figure 18. (Color online.) (a–d) Micromagnetic modeling of the structure and interaction of skyrmions in the conical phase. The dependences of (e) skyrmion–edge and (f) skyrmion–skyrmion distances on the magnetic field. The red and blue dots represent the results of numerical simulations. (g) Field dependences of d_{ss} and d_{se} calculated disregarding magnetostatic fields.

interacting skyrmions is more complex. As seen in Fig. 18d, in the region between the north poles there is always one south pole, which leads to attraction of the skyrmions. In addition, the volume of the pair is less than the total volume of the two isolated CSs in the conical phase. As a result, the total energy of the bound two-skyrmion state will be less than the corresponding energy of the conical phase. However, too small a distance between the two CSs results in an energetically disadvantageous distortion of their spin configurations. Therefore, the competition of two effects leads to an equilibrium distance between skyrmions: (1) a decrease in the total volume of the CS pair; (2) a distortion of each CS.

In [97], a micromagnetic simulation of the behavior of skyrmions in the real geometry of the sample using the MuMax program [101] was also performed. Hamiltonian (20) was used, and the demagnetization fields $\mathbf{B}_d$ at the borders and inside the sample were taken into account. The theoretical curves in Fig. 18e, f (red and blue dots) are in good qualitative and quantitative agreement with the experimental data (white dots). For the critical fields $B_{se} \sim 420$ mT and $B_{ss} \sim 510$ mT, the theoretical dependences for d_{se} and d_{ss} tend to infinity, reflecting the change in the nature of interactions from attraction to repulsion. The reason is that, in a strong external field, the conical phase reaches saturation, and the 'vacuum' surrounding the skyrmions becomes homogeneous and ferromagnetic. As a result, the measured value of the critical field B_{ss} can also be considered the saturation field of the conical phase.

It is important to note that the skyrmion–edge interaction changes character in fields that are significantly smaller than those for the skyrmion–skyrmion interaction. In the field range

$$B_{se} < B_{ext} < B_{ss}\,,$$

skyrmions form clusters that are concentrated in the center of the sample away from the boundaries.

Calculations of d_{se} and d_{ss}, disregarding demagnetization fields, $B_d = 0$ (Fig. 18g), lead not only to a decrease in the critical fields B_{se} and B_{ss}, but also to their equality, $B_{se} = B_{ss}$. This means that the effect of clustering of skyrmions in the center of a sample strongly depends on the demagnetizing field generated by the sample itself. All the above-mentioned effects are also observed in large samples (see the Appendix in [97]). In [97], the potential energy of interaction between skyrmions and also that of a skyrmion with an edge was calculated as the functions of d_{ss} and d_{se}, respectively, calculated for different values of the applied magnetic field. These Lennard-Jones type potentials clearly demonstrate a decrease in the potential well with an increase in the magnetic field.

9. Helical structures in chiral magnets

Helical structures called 'swiss-roll-like vortices' were first observed experimentally [33] in an FeGe helimagnet (Fig. 19a) when the sample was heated to $T > T_N = 280$ K and then cooled to $T = 200$ K. Figure 19b shows an image of such a spin structure obtained by TEM with subsequent TIE processing. A vortex-like unclosed spin strip is clearly visible without a singular point in the center. The spin strip is formed from a helicoidal structure and as a whole twists around a certain center. Schematically, swiss-roll-like vortices are shown in Fig. 19c. A similar pattern of vortex-like spin strips

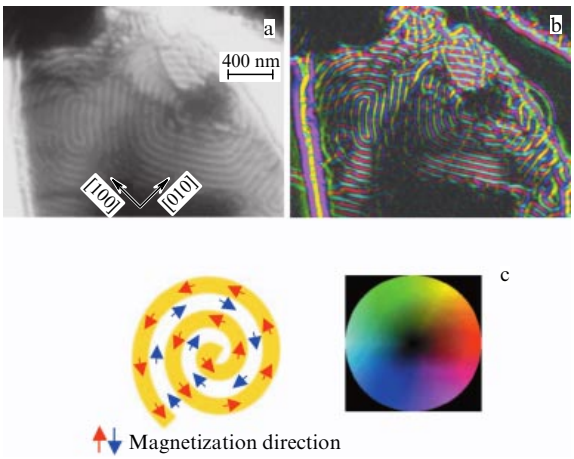

Figure 19. (Color online.) Vortex-like strip spin patterns.

shown in Fig. 19a was observed in other fragments of the sample.

In [102], the structure of these helical textures is studied using analytical and numerical methods in the framework of the standard model. The analytical formula for the structure of a helix outside its core is consistent with numerical calculations and allows us to study the main features of helices, including their behavior in a magnetic field. The Euler–Lagrange equations for the energy functional (15) in the polar coordinate system (r, ϕ) have the form

$$-\left[(\partial_r \Phi)^2 + \frac{\partial_\phi \Phi}{r^2}\right] \sin\theta\cos\theta + \frac{4\pi \sin^2\theta}{L_D}\left[\cos(\phi - \Phi)\partial_r \Phi - \sin(\phi - \Phi)\frac{\partial_\phi \Phi}{r}\right] + \Delta\theta - \frac{4\pi^2 h}{L_D^2}\sin\theta = 0\,, \tag{21}$$

$$\Delta\Phi \sin\theta + 2\left(\frac{\partial_\phi \Phi\, \partial_\phi \theta}{r^2} + \partial_r \Phi\, \partial_r \theta\right)\cos\theta + \frac{4\pi}{L_D}\left[\frac{\partial_\phi \theta}{r}\sin(\phi - \Phi) - \partial_r \theta \cos(\phi - \Phi)\right]\sin\theta\,, \tag{22}$$

where $h = H/H_D$ and Δ is the Laplace operator,

$$\Delta = \frac{\partial^2}{\partial r^2} + \frac{1}{r}\frac{\partial}{\partial r} + \frac{1}{r^2}\frac{\partial^2}{\partial \phi^2}\,.$$

To solve equations (21) and (22), the method of minimizing the energy functional (15) was used. The calculations are performed on a high-density grid selected so that the angle between the directions of two vectors in neighboring nodes does not exceed 10°. The nonlinear method of conjugate gradients with additive penalty functions necessary for fixing the norm of vectors **n** was used. To control the accuracy of the result, the first and second derivatives were calculated, and then the residual of equations (21), (22) was estimated. The algorithm is implemented on the Nvidia CUDA architecture using multiprocessors of video cards (GPUs) for massive parallel computing and real-time visualization. Such technologies can significantly improve the speed and quality of solving a number of computational problems, including micromagnetic ones. As a result, helical structures of various types were found, which are described below.

In addition, based on the analysis of numerical results, it was possible to put through analytical studies. For $r \to \infty$, the asymptotic behavior of solutions of the system (21), (22) for the helical structure was found. So, if $h = 0$, we have

$$\Phi = \frac{\pi}{2} + \phi - \frac{NL_D}{2\pi r} + O\left(\frac{1}{r^2}\right),$$

$$\theta = c_1 - \frac{2\pi}{L_D}\, r + N\phi + O\left(\frac{1}{r}\right),$$

where $N \in \mathrm{Z}$. Here and in the following formulas, the logarithmic terms with arbitrary constants associated with exchange helices, the analytical formula for which is obtained in [103, 104], are omitted. These constants must be set to zero when minimizing the energy (15). Then, the solutions for $n_3 = \cos\theta$ are $2N$ spiral domains separated by Archimedean spirals. It can be shown that for $h > 0$ the asymptotic solution has the form

$$\Phi = \frac{\pi}{2} + \phi - \frac{NL_D}{2\pi r} + O\left(\frac{1}{r^2}\right),$$

$$\theta = \pi - 2\,\mathrm{am}\left[F\left(\frac{\pi - c_1}{2}, m\right) + \frac{2K}{L_D}\, r - \frac{2KN}{\pi}\,\phi + O\left(\frac{1}{r}\right)\right], \qquad r \to \infty\,,$$

where $\mathrm{am}\,(x, m)$ is the Jacobi amplitude, $F(x, m)$ is an incomplete elliptic integral of the 1st kind, and $K = K(m)$ is a complete elliptic integral of the 1st kind. The modulus of elliptic functions and integrals m depends only on h and is determined by the equation (compare with (8))

$$\pi m - 4\sqrt{h}E = 0\,,$$

where $E = E(m)$ is a complete elliptic integral of the 2nd kind. It is noteworthy that the period of spiral turns,

$$L = 4L_D \frac{EK}{\pi^2}\,,$$

coincides with the period of the helicoid (9). At $N = 1$, the $n_3 = \mathrm{const}$ level lines form an Archimedean spiral (AS) (at $N > 1$, the spiral has many branches). As numerical calculations show, spiral textures as metastable states can exist in an environment of labyrinth structures (Fig. 20a, b) or of skyrmions (Fig. 20c, d). Light areas in Fig. 20a–d correspond to the direction of the magnetization vector against the field, and dark ones along the field.

A similar pattern is observed for static spiral domains (SDs) in ferrite-garnet films, which are usually surrounded by a labyrinth domain structure [105] or a lattice of cylindrical magnetic domains [106, 107]. In some samples, they are observed only as dynamic structures [108]. Magnetodipole interactions play a key role in the formation of static SDs [109]. However, for ASs in chiral magnets, as for other solitons with dimensions of the order L_D, accounting for long-range magnetostatic forces is not so critical [64].

Figure 20 shows that an AS is slightly deformed under the influence of the environment. Similar helices for the director field are observed in liquid crystal films [110–112]. However, the director field is highly inhomogeneous along the film thickness and contains topological defects [113]. By contrast, the vector field of ASs is continuous everywhere and has no singularities. Meanwhile, it is topologically nontrivial. When the field increases, the AS period increases, and parts of the helix turns, magnetized against the field, are thinned (see animation [114]). The localized AS (Fig. 20c) due to

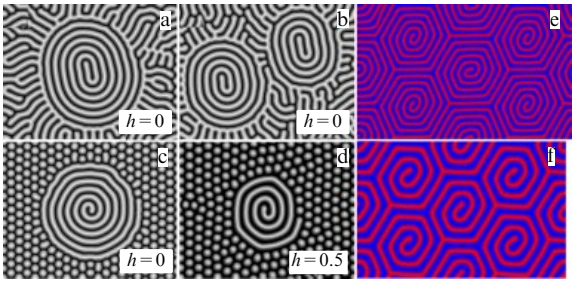

Figure 20. (Color online.) Calculated AS in the environment of various structures: (a, b) the labyrinth structure in the absence of a magnetic field; (c) the skyrmion lattice in the absence of a field; (d) the field $h = 0.5$. The lattice of an AS (e) with five turns in the absence of a magnetic field; (f) with three turns in the field $h = 0.15$.

continuous deformation of the field can be tightened into a two-dimensional skyrmion with a single topological index. For a certain threshold value of the magnetic field, the AS shown in Fig. 20c loses stability and transforms into the same skyrmion as in the surrounding skyrmion lattice.

The existence of single topological defects in condensed matter (dislocations, disclinations, vortices, skyrmions, etc.) is usually accompanied by the formation of their periodic structures. A new equilibrium phase — a hexagonal lattice of Archimedean spirals (LASs) with a different number of turns — was predicted using the method of minimizing the average energy density with periodic boundary conditions. Such structures remain stable at low perturbations and do not transform into a helicoidal phase.

Figures 20e, f show examples of equilibrium lattices of Archimedean spirals. Although this phase superficially resembles the lattice of spiral domains that are observed in ferrite-garnet films [107, 115], its existence is due to the local DM interaction, rather than the long-range and nonlocal magnetostatic interaction.

Numerical analysis of the energies of various two-dimensional structures at zero temperature leads to the following conclusions. In the absence of a magnetic field, the average energy densities (in units E_0/L_D^2) of the Dzyaloshinskii helical phase, AS lattice, and skyrmion lattice are $\sigma_D = -19.74$, $\sigma_{AS} = -19.58$, and $\sigma_s = -18.31$, respectively. The negative sign in expressions for energy densities is associated with the negative sign of the DM energy. In magnetic fields $0 \leqslant h < 0.2$, these energies form a sequence $\sigma_D < \sigma_{AS} < \sigma_s$. At $h \approx 0.2$, the AS lattice becomes unstable. Therefore, the basic state of the system in the form of an AS lattice is possible only at a nonzero temperature and a magnetic field in the range $0 \leqslant h < 0.2$. Under these conditions, the LAS free energy must be lower than the energy of the helicoidal phase, since the spiral lattice has many more degrees of freedom than the one-dimensional helicoid. A metastable AS lattice can be excited by an alternating magnetic field, just as is done for generating metastable spiral domains [115].

10. Conclusion

As noted above, the concept of chiral skyrmions proposed more than 20 years ago turned out to be one of the most important areas in condensed matter physics. Whether it finds promising technical applications will only be shown by future research. We want to believe that familiarity with the review has shown that there are many interesting problems for theorists and experimenters in the field of chiral magnets, and many of their subtle properties are awaiting future research.

We are grateful to V V Kiselev and E A Kravtsov for their careful reading of the manuscript and useful comments, and to D V Dolgikh for his invaluable assistance in its preparation. The work was performed within the framework of the state assignment of the Ministry of Education and Science of Russia (theme Quantum, grant AAAA-A18-118020190095-4).

References

1. Skyrme T H R *Proc. R. Soc. Lond. A* **260** 127 (1961)
2. Skyrme T H R *Proc. R. Soc. Lond. A* **262** 237 (1961)
3. Skyrme T H R *Nucl. Phys.* **31** 556 (1962)
4. Sondhi S L et al. *Phys. Rev. B* **47** 16419 (1993)
5. Khawaja U A Stoof H *Nature* **411** 918 (2001)
6. Fukuda J, Zumer S *Nature Commun.* **2** 246 (2011)
7. Hakonen P J et al. *J. Low Temp. Phys.* **53** 425 (1983)
8. Volovik G E *The Universe in a Helium Droplet* (Oxford: Clarendon Press, 2003)
9. Volovik G E Mineev V P *Sov. Phys. JETP* **46** 401 (1977); *Zh. Eksp. Teor. Fiz.* **73** 767 (1977)
10. Malozemoff A P, Slonczewski J C *Magnetic Domain Walls in Bubble Materials* (New York: Academic Press, 1979); Translated into Russian: *Domennye Stenki v Materialakh s Tsilindricheskimi Magnitnymi Domenami* (Moscow: Mir, 1982)
11. Kosevich A M, Ivanov B A, Kovalev A S *Nelineinye Volny Namagnichennosti. Dinamicheskie i Topologicheskie Solitony* (Nonlinear Waves of Magnetization. Dynamic and Topological Solitons) (Kiev: Naukova Dumka, 1983)
12. Kosevich A M, Ivanov B A, Kovalev A S *Phys. Rep.* **194** 117 (1990)
13. Bogdanov A N, Yablonskii D A *Sov. Phys. JETP* **68** 101 (1989); *Zh. Eksp. Teor. Fiz.* **95** 178 (1989)
14. Ivanov B A, Stephanovich V A, Zhmudskii A A *J. Magn. Magn. Mater.* **88** 116 (1990)
15. Rößler U K et al. *J. Phys. Conf. Ser.* **303** 012105 (2011)
16. Bogdanov A, Hubert A *J. Magn. Magn. Mater.* **138** 255 (1994)
17. Rößler U K, Bogdanov A N, Pfleiderer C *Nature* **442** 797 (2006)
18. Bogdanov A, Hubert A *J. Magn. Magn. Mater.* **195** 182 (1999)
19. Bogdanov A N, Rössler U K, Pfleiderer C *Physica B* **359** 1162 (2005)
20. Yu X Z et al. *Nature* **465** 901 (2010)
21. Seidel J (Ed.) *Topological Structures in Ferroic Materials: Domain Walls, Vortices and Skyrmions* (Springer Series in Materials Science, Vol. 228) (Berlin: Springer, 2016)
22. Seki S, Mochizuki M *Skyrmions in Magnetic Materials* (Cham: Springer, 2016)
23. Han J H *Skyrmions in Condensed Matter* (Springer Tracts in Modern Physics, Vol. 278) (Cham: Springer, 2017)
24. Liu J P, Zhang Z, Zhao G (Eds) *Skyrmions: Topological Structures, Properties, and Applications* (Boca Raton, FL: CRC Press, 2017)
25. Gupta S, Saxena A (Eds) *The Role of Topology in Materials* (Springer Series in Solid-State Sciences, Vol. 189) (Cham: Springer, 2018)
26. Stishov S M, Petrova A E *Phys. Usp.* **60** 1268 (2017); *Usp. Fiz. Nauk* **187** 1365 (2017)
27. Izyumov Yu A *Sov. Phys. Usp.* **27** 845 (1984); *Usp. Fiz. Nauk* **144** 439 (1984)
28. Fert A, Reyren N, Cros V *Nature Rev. Mater.* **2** 17031 (2017)
29. Nagaosa N, Tokura Y *Nature Nanotechnol.* **8** 899 (2013)
30. Finocchio G et al. *J. Phys. D* **49** 423001 (2016)
31. Bihlmayer G et al. "Magnetic skyrmions: structure, stability, and transport phenomena", ψ_k Scientific Highlight of the Month (139) (2018), https://psi-k.net/download/highlights/Highlight_139.pdf
32. Rybakov F N et al. *Phys. Rev. Lett.* **115** 117201 (2015)
33. Uchida M et al. *Phys. Rev. B* **77** 184402 (2008)
34. Dzyaloshinskii I E *Sov. Phys. JETP* **20** 665 (1965); *Zh. Eksp. Teor. Fiz.* **47** 992 (1964)
35. Moriya T *Phys. Rev.* **120** 91 (1960)
36. Bak P, Jensen M H *J. Phys. C* **13** L881 (1980)

37. Izyumov Yu A *Difraktsiya Neitronov na Dlinnoperiodicheskikh Strukturakh* (Neutron Diffraction on Long-Period Structures) (Moscow: Energoatomizdat, 1987)
38. Chizhikov V A, Dmitrienko V E *Phys. Rev. B* **85** 014421 (2012)
39. Ishikawa Y et al. *Solid State Commun.* **19** 525 (1976)
40. Maleyev S V *Phys. Rev. Lett.* **75** 4682 (1995)
41. Grigoriev S V et al. *Phys. Rev. B* **73** 224440 (2006)
42. Grigoriev S V et al. *Phys. Rev. B* **76** 092407 (2007)
43. Grigoriev S V et al. *Phys. Rev. B* **76** 224424 (2007)
44. Grigoriev S V et al. *Phys. Rev. B* **74** 214414 (2006)
45. Grigoriev S V et al. *Phys. Rev. Lett.* **102** 037204 (2009)
46. Uchida M et al. *Science* **311** 359 (2006)
47. Bajt S et al. *Ultramicroscopy* **83** 67 (2000)
48. Uchida M et al. *Appl. Phys. Lett.* **86** 131913 (2005)
49. Ishimoto K et al. *Physica B* **213–214** 381 (1995)
50. Beille J, Voiron J, Roth M *Solid State Commun.* **47** 399 (1983)
51. Kittel Ch *Introduction to Solid State Physics* (New York: Wiley, 1971); Translated into Russian: *Vvedenie v Fiziku Tverdogo Tela* (Moscow: Nauka, 1978)
52. Bogdanov A N, Rössler U K, Pfleiderer C *Physica B* **359** 1162 (2005)
53. Mühlbauer S et al. *Science* **323** 915 (2009)
54. Münzer W et al. *Phys. Rev. B* **81** 041203(R) (2010)
55. Butenko A B et al. *Phys. Rev. B* **82** 052403 (2010)
56. Wilson M N et al. *Phys. Rev. B* **89** 094411 (2014)
57. Wilson M N et al. *Phys. Rev. B* **86** 144420 (2012)
58. Seki S et al. *Science* **336** 198 (2012)
59. Huang S X, Chien C L *Phys. Rev. Lett.* **108** 267201 (2012)
60. Yu X Z et al. *Nature Mater.* **10** 106 (2011)
61. Yu X Z et al. *Nature Commun.* **3** 988 (2012)
62. Tonomura A et al. *Nano Lett.* **12** 1673 (2012)
63. Rybakov F N, Borisov A B, Bogdanov A N *Phys. Rev. B* **87** 094424 (2013)
64. Kiselev N S et al. *J. Phys. D* **44** 392001 (2011)
65. Helimagnets. YouTube, http://www.youtube.com/user/helimagnets
66. Meynell S A et al. *Phys. Rev. B* **90** 014406 (2014)
67. Wilson M N et al. *Phys. Rev. B* **88** 214420 (2013)
68. Song D et al. *Phys. Rev. Lett.* **120** 167204 (2018)
69. Rybakov F N et al. *New J. Phys.* **18** 045002 (2016)
70. Leonov A O et al. *Phys. Rev. Lett.* **117** 087202 (2016)
71. Parkin S, Yang S-H *Nature Nanotechnol.* **10** 195 (2015)
72. Fert A, Cros V, Sampaio J *Nature Nanotechnol.* **8** 152 (2013)
73. Müller J *New J. Phys.* **19** 025002 (2017)
74. Shibata K et al. *Nature Nanotechnol.* **8** 723 (2013)
75. Romming N et al. *Science* **341** 636 (2013)
76. Ray M W et al. *Nature* **505** 657 (2014)
77. Castelnovo C R, Moessner R, Sondhi S L *Nature* **451** 42 (2008)
78. ChiralBobber. YouTube, https://www.youtube.com/channel/UCN4mgZGR4Yv3T9Yc-94RDAA
79. Volovik G E, Mineev V P *Fizika i Topologia* (Physics and Topology) (New in Life, Science, and Technology. Ser. Physics, Issue 6) (Moscow: Znanie, 1980)
80. Blaha S *Phys. Rev. Lett.* **36** 874 (1976)
81. Volovik G E, Mineev V P *JETP Lett.* **23** 593 (1976); *Pis'ma Zh. Eksp. Teor. Fiz.* **23** 647 (1976)
82. Mineyev V P, Volovik G E *Phys. Rev. B* **18** 3197 (1978)
83. Ollikainen T et al. *Phys. Rev. X* **7** 021023 (2017)
84. Borisov A B, Tankeev A P, Shagalov A G *Phys. Solid State* **31** 798 (1989); *Fiz. Tverd. Tela* **31** (5) 140 (1989)
85. Volovik G E, Mineev V P *Sov. Phys. JETP* **45** 1186 (1977); *Zh. Eksp. Teor. Fiz.* **72** 2256 (1977)
86. Bessarab P F, Uzdin V M, Jónsson H *Comput. Phys. Commun.* **196** 335 (2015)
87. Zheng F et al. *Nature Nanotechnol.* **13** 451 (2018)
88. Feinberg E L *Sov. Phys. Usp.* **5** 753 (1963); *Usp. Fiz. Nauk* **78** 53 (1962)
89. Midgley P A, Dunin-Borkowski R E *Nature Mater.* **4** 271 (2009)
90. Milde P et al. *Science* **340** 1076 (2013)
91. Schütte C, Rosch A *Phys. Rev. B* **90** 174432 (2014)
92. Leonov A O et al. *J. Phys. Condens. Matter* **28** 35LT01 (2016)
93. Ahmed A S et al. *Phys. Rev. Mater.* **2** 041401(R) (2018)
94. Weller D, Moser A *IEEE Trans. Mag.* **35** 4423 (1999)
95. Du H et al. *Nature Commun.* **6** 8504 (2015)
96. Bogdanov A *JETP Lett.* **62** 247 (1995); *Pis'ma Zh. Eksp. Teor. Fiz.* **62** 231 (1995)
97. Du H et al. *Phys. Rev. Lett.* **120** 197203 (2018)
98. Shibata K et al. *Phys. Rev. Lett.* **118** 087202 (2017)
99. Du H et al. "Jumps of skyrmion", Interaction of Individual Skyrmions. YouTube, https://www.youtube.com/watch?v = vmnBtIbrI1U
100. Du H et al. "Field-driven motion of skyrmions (magnetization/demagnetization)", Interaction of Individual Skyrmions. YouTube, https://www.youtube.com/watch?v = YHweP452Z24&t = 5s
101. Vansteenkiste A et al. *AIP Adv.* **4** 107133 (2014)
102. Borisov A B, Rybakov F N *JETP Lett.* **96** 521 (2012); *Pis'ma Zh. Eksp. Teor. Fiz.* **96** 572 (2012)
103. Borisov A B *JETP Lett.* **73** 242 (2001); *Pis'ma Zh. Eksp. Teor. Fiz.* **73** 279 (2001)
104. Borisov A B *JETP Lett.* **76** 84 (2002) *Pis'ma Zh. Eksp. Teor. Fiz.* **76** 95 (2002)
105. Ges' A P et al. *JETP Lett.* **52** 476 (1990); *Pis'ma Zh. Eksp. Teor. Fiz.* **52** 1079 (1990)
106. Lamonova K V, Mamalui Yu A, Siryuk Yu A *Fiz. Tekh. Vys. Davl.* **6** (1) 33 (1996)
107. Mamalui Ju A, Siryuk Ju A *Bull. Russ. Acad. Sci. Phys.* **72** 1026 (2008); *Izv. Ross. Akad. Nauk Ser. Fiz.* **72** 1091 (2008)
108. Kandaurova G S *Phys. Usp.* **45** 1051 (2002); *Usp. Fiz. Nauk* **172** 1165 (2002)
109. Borisov A B, Yalyshev Yu I *Fiz. Met. Metalloved.* **79** (5) 18 (1995)
110. Gilli J M, Kamayé M *Liquid Cryst.* **11** 791 (1992)
111. Mitov M, Sixou P *J. Phys. II France* **2** 1659 (1992)
112. Ribiere P, Oswald P, Pirkl S *J. Phys. II France* **4** 127 (1994)
113. Oswald P, Baudry J, Pirkl S *Phys. Rep.* **337** 67 (2000)
114. "Archimedian spiral", NonlinearPhenomena. YouTube, https://www.youtube.com/watch?v = LVapNv850OA
115. Mamalui Yu A, Soika E N *Phys. Status Solidi A* **184** 437 (2001)